ChemCatChem

Research Article
doi.org/10.1002/cctc.202401511

Chemistry Europe
European Chemical Societies Publishing

www.chemcatchem.org

Novel Heterogeneous Pd Catalysts for Cross-Coupling Reactions in Biocompatible Media: Structural Insights from Solid-State NMR Techniques

Till Wissel,[a] Lorenz Rösler,[a] Martin Brodrecht,[a, b] Mark V. Höfler,[a] Kevin Herr,[a] Marcos de Oliveira Jr.,[c] Vytautas Klimavicius,[d] Martin Ebert,[e] Hergen Breitzke,[a] Markus Hoffmann,[f] Gerd Buntkowsky,*[a] and Torsten Gutmann*[a]

Novel SBA-15-supported heterogeneous catalysts are synthesized and applied in the Mizoroki–Heck and the Suzuki–Miyaura cross-coupling reactions in green solvents like PEG or water. The structural properties of the products after each synthesis step are monitored by different analytics. The amount of amine/carboxyl groups and vanillin/histidine methyl ester and thermal stability are determined by TGA and elemental analysis, while ICP-OES delivered the amount of palladium of the catalysts. The morphology is investigated by SEM and XPS and confirms the presence of coordinated palladium in the zero-oxidation state. Gas adsorption analysis is conducted, which indicates the presence of palladium clusters in one of the two catalysts, which is underlined by BSE images combined with EDX. A detailed ^{13}C ssNMR and DNP-enhanced ^{15}N ssNMR spectral analysis is presented, which provides ultimate proof of the successful syntheses of the catalysts. The coordination of the palladium onto the carrier material is shown by combining the NMR spectral results with the results of the other analytics. First catalytic tests show for the Mizoroki–Heck reaction yields up to nearly 100% and for the Suzuki-Miyaura up to 88% in the presence of PEG and water, respectively.

1. Introduction

Transition metal-catalyzed cross-coupling reactions are of broad interest for synthesis of organic compounds since they allow the direct formation of carbon–carbon bonds,[1–12] which is otherwise difficult to achieve.[5,8,10,13] Thus, Heck, Negishi, and Suzuki were awarded a Nobel Prize in 2010 for their pioneering works establishing such cross-coupling reactions.[2,14] Since the 1970s, various palladium-catalyzed reactions have been developed,[15–17] a research field that is still very active today.[2,5,13,18] In particular, Suzuki reactions are widely used in pharmaceutical industry,[19–24] while the Heck reaction is an important synthetic tool for manufacturing fine chemicals.[25–31] Prominent examples of ton-scale products that are produced with the help of cross-coupling reactions are Naproxen,[31] which is a nonsteroidal anti-inflammatory drug, and Valsartan,[32] which treats high blood pressure, heart failure, and diabetic kidney disease, respectively.

Typically, cross-coupling reactions require a transition metal catalyst, where palladium-containing ones have been considered to be the most efficient.[1–3,10,33–35] Homogeneous catalysts are often used for these transformations since they possess high activity and selectivity. Such catalysts, however, pose major challenges concerning their separation from the product and recovery.[6] This becomes even more critical in manufacturing processes of pharmaceuticals, where remaining metal traces lead to contamination.[36] Furthermore, palladium is a metal that is only available in limited quantities on earth, so there is a high demand for efficient recovery. A solution that addresses these challenges is the use of heterogeneous catalysts, which, however, often suffer from low activity and selectivity. To overcome the low activity and selectivity, homogeneous catalysts have been immobilized on solid support material in the past.[7,11,37–43] There are various solid supports, such as carbon,[3] polymers,[44] cellulose,[36] metal oxides,[45] and porous silica,[7] that are suit-

[a] T. Wissel, L. Rösler, M. Brodrecht, M. V. Höfler, K. Herr, H. Breitzke, G. Buntkowsky, T. Gutmann
Institute of Inorganic and Physical Chemistry, Technical University of Darmstadt, Peter-Grünberg-Straße 8, Darmstadt D-64287, Germany
E-mail: gerd.buntkowsky@chemie.tu-darmstadt.de
gutmann@chemie.tu-darmstadt.de

[b] M. Brodrecht
Dr. Robert-Murjahn-Institut GmbH (RMI), Industriestraße 12, Ober-Ramstadt D-64372, Germany

[c] M. de Oliveira Jr.
São Carlos Institute of Physics, University of São Paulo, São Carlos, São Paulo 13560-970, Brazil

[d] V. Klimavicius
Institute of Chemical Physics, Vilnius University, Vilnius LT-10257, Lithuania

[e] M. Ebert
Institute of Applied Geosciences, Technical University Darmstadt, Schnittspahnstraße 9, Darmstadt D-64287, Germany

[f] M. Hoffmann
Department of Chemistry and Biochemistry, State University of New York College at Brockport, Brockport, New York 14420, USA

Supporting information for this article is available on the WWW under https://doi.org/10.1002/cctc.202401511

able. Among these, porous silica has drawn much attention due to its chemical and mechanical stability, high surface area, ecofriendly synthesis, ability of surface modifications by numerous linkers, tunability of the pore architecture, and recovery by filtration or centrifugation.[9,11,46]

Although many studies have dealt with the immobilization of homogeneous catalysts on porous silica, there is still a need to develop novel systems to address current demands. Especially, there is an increasing interest in sustainable chemistry summarized as the principles of green chemistry.[47,48] In this regard, catalysts are not only required to show high catalytic performance, easy separation, and recovery, but they also need to be applicable in nontoxic environmentally friendly solvents such as water or polyethylene glycol (PEG).[48,49]

Even though, in the literature, several interesting approaches to these demands are reported (for examples, see the reviews by Sharma and Singh[21] or by Christoffel and Ward[14]), the mechanism of Pd-catalyzed reactions employing immobilized catalysts is not well understood in the context of reactions in green solvents.[2,50,51] In particular, confinement effects of porous support material have not been discussed in detail even though these may play a crucial role in understanding catalytic activity.[52] Thus, there is a pressing need to understand the role of the solvent in heterogeneous Pd catalysis, as well as the confinement effects in porous support materials relevant for catalysis with immobilized transition metal catalysts.

For a detailed analysis of the reaction mechanism, the catalyst system requires a tunable, well-defined structure that is fully characterized. While the synthesis of immobilized catalysts is well established and can be performed in a reproducible way, detailed analytics is a challenging task. Several techniques, such as X-ray diffraction (XRD), infrared spectroscopy (IR), or electron microscopy, are commonly used to obtain information on structural order as well as to identify chemical moieties.[53] However, these techniques do not provide detailed information on local structures that are mandatory to interpret observations in mechanism studies. For this purpose, ssNMR has been well established for a number of supported catalysts (see reviews and references therein).[54–63] However, when catalysts with small surface loading or nuclei such as ^{15}N with low sensitivity in natural abundance need to be investigated, the ssNMR approach suffers from its low intrinsic sensitivity. A solution to overcome this drawback is the use of DNP-enhanced ssNMR. This technique transfers the three order of magnitude higher polarization of electron spins to the desired nuclear spin polarization. This enables the detection of nuclei in natural abundance even if they are present in small amounts.[64–67] Finally, DNP-enhanced ssNMR can also be used as a powerful tool to investigate the dynamics of solvents inside confinements, as shown by some of the authors.[68–74]

In this work, we present two synthesis approaches that run under mild conditions with mostly nontoxic chemicals to immobilize a well-defined commercial palladium catalyst (palladium(II) acetate) with the help of natural products acting as anchors on SBA-15 (see Scheme 1). Such model catalysts may be applied for solvent dynamic investigations and mechanistic studies. The first approach uses a Schiff base complex with the natural product vanillin. In this case, the vanillin is attached to the silica surface via an imine bond between the aldehyde group of the vanillin and a (3-aminopropyl)triethoxysilane (APTES) linker attached to the silica surface. The second approach uses a histidine methyl ester, which is anchored to the surface by an amide bond between the amine group of the histidine methyl ester and a carboxyethylsilanetriol disodium salt (CES) linker attached to the silica surface.

The two modified silica materials are then used to immobilize palladium acetate. Each synthesis step of the two approaches is monitored by combining characterization techniques such as EA, TGA, ICP-OES, SEM, XPS, and gas adsorption analysis. Special focus is set on ssNMR and DNP-enhanced ssNMR to determine local structures and to investigate the coordination of the Pd. Finally, both catalysts are applied in a Mizoroki–Heck reaction between iodobenzene and styrene and Suzuki–Miyaura cross-coupling reaction between iodobenzene and phenylboronic acid as model reactions in water and PEG to test their catalytic performance.

2. Experimental Details

2.1. General

If not explicitly mentioned, all chemicals were used without any further purification. Pluronic P123 (M_n ~5800), vanillin (98%), palladium(II) acetate (98%), sodium borohydride (≥98%, $NaBH_4$), 2-pyridinol-1-oxid (≥98%, HOPO), L-histidine methyl ester dihydrochloride (97%), *trans*-α-methylstilbene (99%), styrene (≥99%), potassium carbonate (99%, K_2CO_3), phenylboronic acid (≥97%), methanol (≥99.9%), and dichloromethane (≥99.9%, DCM) were purchased from Sigma-Aldrich. Hydrochloric acid (37 wt%, HCl), sulfuric acid (96%), *N*,*N*′-diisopropylcarbodiimide (≥99%, DIC), ethanol (≥99.8%, EtOH), and magnesium sulfate monohydrate (≥99%) were purchased from Carl Roth. (3-aminopropyl)triethoxysilane (98%, APTES) and carboxyethylsilanetriol disodium salt (25 wt% in H_2O, CES) were purchased from ABCR. Tetraethyl ortho silicate (98%, TEOS) and iodobenzene (98%) were purchased from Acros. Polyethylene glycol 400 (PEG-400) and *cis*-stilbene (97%) were purchased from Alfa Aesar. 4-methylbiphenyl (>98%) and *trans*-stilbene (>98%) were purchased from TCI. Biphenyl (99%) was purchased from Merck and acetonitrile (>99.9%, MeCN) from VWR.

Before the mesoporous silica material was used for immobilization, it was dried under high vacuum for at least 12 h. Toluene was bought dry, while ethanol was dried for at least 1 week in a baked-out flask under argon atmosphere with a 3 Å molecular sieve.

2.2. Synthesis of Catalyst A (VII)

2.2.1. Synthesis of APTES-Functionalized SBA-15 (SBA-NH_2/III)

The synthesis is based on an optimized protocol described by Wang et al.[75] and Zeidan et al.[76] In a typical procedure, 21.3 g (3.7 mmol, 0.017 equiv.) Pluronic P123 was dissolved in 574 mL

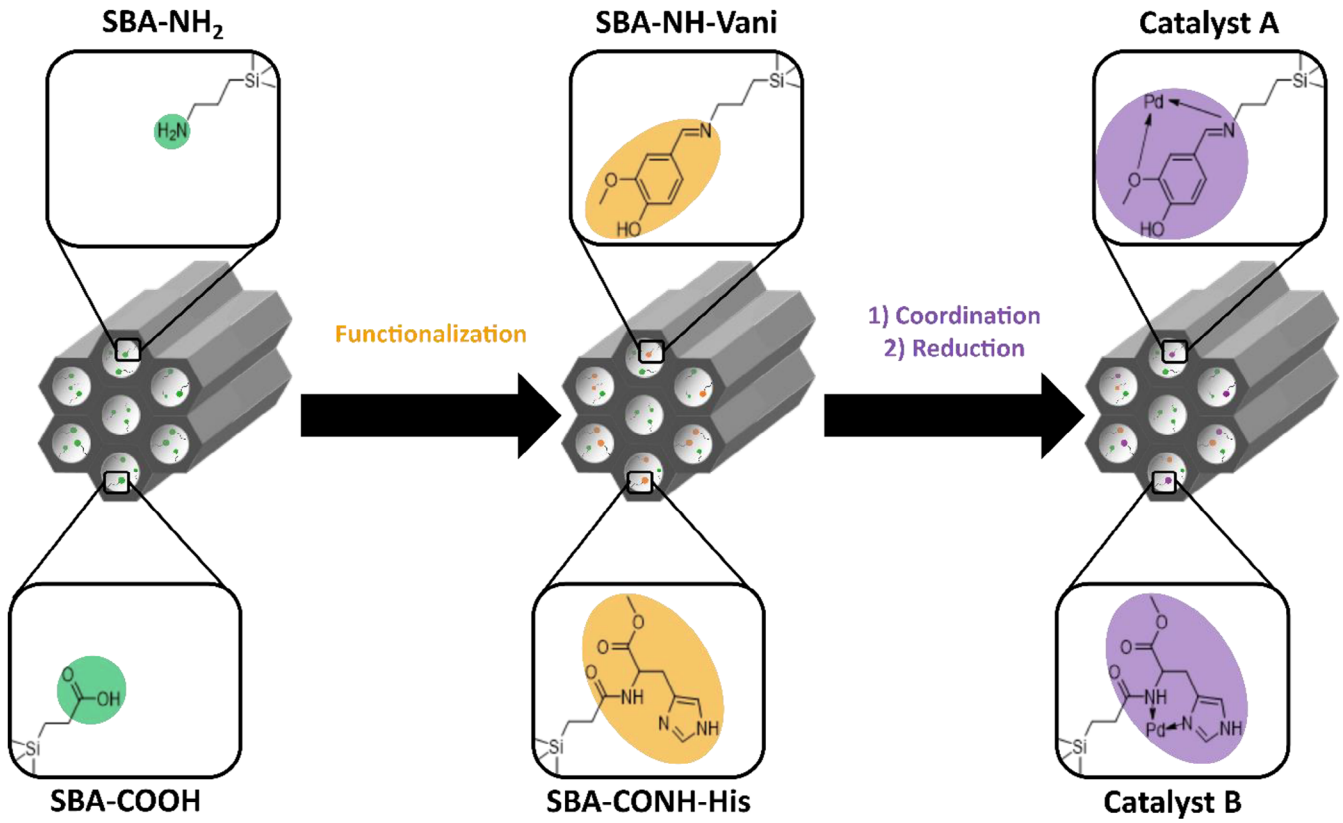

Scheme 1. Schematic illustration of the two synthesis approaches. Both start with the synthesis of SBA-15 with the corresponding linker (depicted in green) followed by the functionalization with the anchor molecule (depicted in orange) and finish with the coordination of the palladium and its reduction (depicted in purple). Note: The synthesis route with the amine linker and vanillin as the anchor (upper half) is denoted as catalyst A, while the route with the carboxylic linker and histidine (lower half) is denoted as catalyst B.

(35.6 mol, 165 equiv.) deionized water, and 108 mL HCl (1.3 mol, 6 equiv., 37 wt%) was added. The solution was heated to 40 °C and stirred for 48 h. Subsequently, 36 g (172.8 mmol, 0.8 equiv.) TEOS (**I**) was slowly added dropwise, and the suspension was stirred at 40 °C for 4 h. After the pre-hydrolysis step, 9.6 g (43.2 mmol, 0.2 equiv.) APTES (**II**) was added, and the suspension was stirred for another 24 h. The suspension was transferred into a Teflon bottle and aged for 48 h at 90 °C under static conditions. Continuing, the mixture was centrifuged (5 min at 4500 rpm), and the supernatant solution decanted. The white precipitate was swirled with deionized water and centrifuged again. This pre-washing procedure was repeated five times. For the complete removal of the template, the wet, crude product was purified via Soxhlet extraction with ethanol for 3 days. The white product was pre-dried at room temperature and fully dried under high vacuum, yielding 11 g of APTES-functionalized SBA-15 (**III**).

2.2.2. Synthesis of Vanillin-Functionalized SBA-15 (SBA-NH-Vani/V)

The synthesis is based on a modified protocol by Khanmoradi et al.[37] Typically, 3.7 g (24 mmol, 2.4 equiv.) vanillin (**IV**) was dissolved in 100 mL of dry toluene, and 5 g (10 mmol loading of amine groups, 1 equiv.) of the dried APTES-functionalized SBA-15 (**III**) was added. The suspension was stirred under reflux with a Dean–Stark apparatus for 72 h. The solid was filtered off, washed three times with toluene and ethanol each, and dried under high vacuum, yielding 5.9 g of the vanillin-functionalized SBA-15 (**V**) as yellow powder.

2.2.3. Immobilization of Palladium Acetate on Vanillin-Functionalized SBA-15 (Catalyst A/VII)

The synthesis is based on a modified protocol by Khanmoradi et al.[37] Typically, 2 g (2 mmol loading of vanillin, 1 equiv.) dried vanillin-functionalized APTES SBA-15 (**V**) was refluxed together with 1.1 g (5 mmol, 2.5 equiv.) palladium(II) acetate (**VI**) in 50 mL of dry ethanol. To reduce the palladium to the zero-oxidation state, 63.1 mg (1.7 mmol, 0.3 equiv.) $NaBH_4$ was added after 20 h, and the reaction was continued for another 2 h. The black solid was filtered off, washed several times with ethanol, and dried under high vacuum, yielding 2.2 g of the palladium catalyst A (**VII**).

2.3. Synthesis of Catalyst B (XII)

2.3.1. Synthesis of Carboxyl-Functionalized SBA-15 (SBA-COOH/IX)

The synthesis is based on a modified protocol by Tsai et al.[77] In a typical procedure, 4 g (0.7 mmol, 0.017 equiv.) Pluronic P123 was dissolved in 106 mL (6.6 mol, 162.7 equiv.) deionized water, and

19.9 mL (238.4 mmol, 5.9 equiv., 37 wt%) HCl was added. The solution was heated to 40 °C and stirred for 4 h. A pre-mixed solution of 5.1 g (24.2 mmol, 0.6 equiv.) TEOS (**I**) and 12.7 g (16.2 mmol, 0.4 equiv., 25 wt%) CES (**VIII**) was slowly added dropwise to the reaction solution. Subsequently, the mixture was vigorously stirred at 40 °C for 20 h. The white suspension was transferred into a Teflon bottle and aged under static conditions for 24 h at 100 °C. Continuing, the mixture was centrifuged (5 min at 4500 rpm), and the supernatant solution decanted. The white precipitate was swirled with deionized water and centrifuged again. This pre-washing procedure was repeated five times. For complete removal of the template, the wet, crude product was stirred at 95 °C in 500 mL of 48 wt% sulfuric acid for 24 h. The white solid was filtered off and washed until the eluent reached a neutral pH value. The white powder was dried under high vacuum, yielding 3.8 g of carboxyl-functionalized SBA-15 (**IX**).

2.3.2. Synthesis of Histidine-Functionalized SBA-15 (SBA-CONH-His/XI)

66.7 mg (0.6 mmol, 1.1 equiv.) HOPO was dissolved in 4.5 mL of MeCN. Subsequently, 150 mg (0.57 mmol loading of carboxylic groups, 1 equiv.) of the carboxylic-functionalized SBA-15 (**IX**) and 113.6 mg (0.9 mmol, 1.6 equiv.) DIC were added, and the suspension was shaken for 1 min. In the meantime, 290.5 mg (1.2 mmol, 2.1 equiv.) histidine methyl ester dihydrochloride (**X**) was dissolved in 250 µL of deionized water. After shaking, the complete amino acid solution was added to the reaction mixture. The suspension was shaken overnight, the solid was filtered off, and washed several times with deionized water. The product was dried under high vacuum, yielding 147.9 mg histidine-functionalized SBA-15 (**XI**).

2.3.3. Immobilization of Palladium Acetate on Histidine-Functionalized SBA-15 (Catalyst B/XII)

The synthesis is based on a modified protocol by Hajipour et al.[38] Typically, 90 mg (0.08 mmol loading of histidine, 1 equiv.) of dried histidine-functionalized SBA-15 (**XI**) was stirred together with 49.4 mg (0.2 mmol, 2.4 equiv.) of palladium(II) acetate (**VI**) in 20 mL of deionized water at room temperature. To reduce the palladium to the zero-oxidation state, 4.2 mg (0.1 mmol, 1.2 equiv.) $NaBH_4$ was added after 24 h, and the reaction was continued for another 2 h. The black solid was filtered off, washed several times with ethanol, and dried under high vacuum, yielding 98.3 mg of catalyst B (**XII**).

2.4. Basic Characterization

2.4.1. X-Ray Photoelectron Spectroscopy (XPS)

A SSX 100 ESCA spectrometer from Surface Science Laboratories Inc. was used for the analyses. The monochromatic X-ray radiation was produced by an Al-K_α source with an energy of 1486.6 eV, and the detection was performed with an angle of 36° under constant analyzer energy. The irradiated area was 0.25 mm × 1.00 mm. The spectra for the bonding energy were recorded at room temperature with a pass energy of 50 eV, a resolution of 0.1 eV, and data points were recorded in 0.1 eV steps. The binding energies were corrected with the C1 s peak. The spectra were evaluated with the CasaXPS software.

2.4.2. Scanning Electron Microscopy (SEM)

For the SEM images, an XL30-FEG electron microscope from Philips was used. Before recording the images, all samples were coated with gold using the sputter coater Quorum Q300T D for 100 s with 30 mA in an argon atmosphere. The acceleration voltage amounted to 15 kV with a spot size of 3.

For the elemental mappings and the referring BSE images, a FEI ESEM Quanta 400F (Eindhoven, The Netherlands) equipped with a X max 80 energy-dispersive X-ray (EDX) detector (Oxford Instruments, Abingdon, UK) was used. All investigations were carried out at 15 kV acceleration voltage and with a spot size of 5.

2.4.3. Thermogravimetric Analysis (TGA)

Thermogravimetric analyses were performed with a TG 209 F3 Tarsus from NETZSCH. For an analysis, approximately 5 mg of the substance was weighed into an aluminum oxide crucible. The sample was heated up from 40 to 100 °C, and the temperature was held for 80 min as a pre-drying step. Afterwards, the temperature was raised to 700 °C and held for 30 min to ensure complete degradation of the organic compounds. The heating rate was set to 20 K min^{-1}.

2.4.4. Elemental Analysis (EA)

A VarioEL III CHN from Elementar was used to perform elemental analyses. The sample (1–3 mg) got combusted in tin capsules under O_2 atmosphere. In an analysis, nitrogen oxidizes to NO_X, which gets reduced by elemental copper, while carbon oxidizes to CO_2 and hydrogen to H_2O. After separation of the gases by gas chromatography, they were quantified by a thermal conductivity detector (TCD). Helium served as a carrier gas, and acetanilide was used for calibration.

2.4.5. Gas Adsorption Analysis

A Thermo Fisher Scientific Surfer Brunauer–Emmett–Teller (BET) analyzer was used to characterize the porosity and specific surface area of the mesoporous materials. The analyses were performed at 77 K using nitrogen as adsorptive. The specific surface area was obtained by applying the BET model and analyzing the curve of the gas adsorption isotherms in the p/p^0 range between 0.03 and 0.3. The pore volume was determined at the p/p^0 value of 0.95 with the help of the Gurvich method. The pore size distribution was obtained by applying the Barett–Joyner–Halenda (BJH) method at the desorption branch in the p/p^0 range between 0.2 and 0.95 with the *t*-plot of de Boer. In addition to the BJH method, the NLDFT method at 77 K for cylindrical silica with nitrogen adsorption was used to determine the pore diameter.

2.4.6. Inductively Coupled Plasma Optical Emission Spectrometry (ICP-OES)

ICP-OES analyses were performed by the AZBA GmbH according to their protocol DIN EN ISO 11885:2009-09.

2.4.7. Solid-State NMR Experiments

The standard solid-state NMR spectra were measured at room temperature on a Bruker AVANCE II+ 400 MHz spectrometer, corresponding to frequencies of 400.13 MHz for ^{1}H and 100.61 MHz for ^{13}C. For experiments, a 4 mm double resonance probe was employed. Spectra were recorded with cross-polarization (CP) employing a contact time of 1.5 ms with a recycle delay of 2 s. The tppm20 decoupling sequence[78] was applied to decouple protons during data acquisition. Spectra were referenced to tetramethylsilane (TMS, 0 ppm) employing adamantane (−38.5 ppm) as an external standard.

2.4.8. DNP-Enhanced Solid-State NMR Experiments

Samples for DNP-enhanced $^{1}H\rightarrow{}^{15}N$ CP MAS measurements were prepared by impregnating a solid sample with a solution of 15 mM TOTAPOL in D_2O/H_2O (9:1) (for sample SBA-NH_2 (**III**)) or 15 mM AMUPol in DMSO-d_6/DMSO (9:1) (for samples SBA-NH-Vani (**V**), catalyst A (**VII**), histidine methyl ester (**X**), SBA-CONH-His (**XI**), and catalyst B (**XII**)). Typically, 15 mg of the solid sample was mixed with 15 µL of the solution containing the radical. Subsequently, they were filled in a 3.2 mm sapphire rotor and sealed with a Teflon plug and ZrO_2 driving cap.

All experiments were carried out on a Bruker AVANCE III spectrometer equipped with an Ascend 400 DNP magnet and a $^{1}H/X/Y$ low-temperature probe that works at frequencies of 400.03 MHz for ^{1}H and 40.54 MHz for ^{15}N. Spectra were recorded at nominally 110 K with microwave radiation (MW on) at a spinning rate of 8 kHz (samples **III, V, VII, X,** and **XI**) or 10 kHz (**XII**), respectively. The $^{1}H\rightarrow{}^{15}N$ CP MAS spectra were recorded employing a 2.75 µs excitation pulse on ^{1}H followed by a 50–100 ramp with a contact time of 4–5 ms. The recycle delay was set to 1.3 t_B, where t_B is the built-up time for ^{1}H obtained with microwave irradiation for each individual sample. Between 16 k and 180 k scans were accumulated to obtain the spectra. The tppm20 decoupling sequence[78] was applied to decouple protons during data acquisition. Spectra were referenced to NH_4Cl (0 ppm) as an external standard.

2.4.9. Catalytic Tests

Stock solutions were prepared to guarantee the same amounts of reactants in the catalytic tests. They were stored in the freezer to avoid evaporation of the solvent and thus to preserve stable concentration over time.

K_2CO_3 stock solution (stock solution A): 8.3 g (60 mmol) K_2CO_3 was weighed in a 10 mL volumetric flask, and the flask was filled with deionized water to the 10 mL mark to dissolve K_2CO_3 resulting in a concentration of 6 mol L^{-1}.

Iodobenzene and styrene stock solution (stock solution B): Iodobenzene (10.4 g (51 mmol)) and 7.9 g (75.9 mmol) of styrene were weighed together in a 20 mL volumetric flask, and the flask was filled to the 20 mL mark with methanol, resulting in a concentration of 2.6 mol L^{-1} for iodobenzene and 3.8 mol L^{-1} for styrene, respectively.

2.4.10. Model Reaction 1: Mizoroki–Heck Cross-Coupling

In a round-bottom flask, 400 µL stock solution B (1 mmol iodobenzene, 1 equiv., 1.5 mmol styrene, 1.5 equiv.), 500 µL stock solution A (3 mmol K_2CO_3, 3 equiv.), and 213.7 mg (1.1 mmol, 1.1 equiv.) *trans*-α-methylstilbene were mixed with 2.6 mL of PEG-400 and heated to 150 °C (see Figure 9A1). After 5 min, when the temperature was achieved, 1.5 mg ($3/3.2 \times 10^{-3}$ mmol Pd, 0.002 equiv.) of catalyst A (**VII**) or B (**XII**), respectively, was added to the solution. The reaction was monitored by GC until iodobenzene was completely converted.

2.4.11. Model Reaction 2: Suzuki–Miyaura Cross-Coupling

In a round-bottom flask, 500 µL of stock solution A (3 mmol K_2CO_3, 3 equiv.), 208.2 mg (1 mmol, 1 equiv.) iodobenzene, 213.7 mg (1.1 mmol, 1.1 equiv.) 4-methylbiphenyl, and 138.3 mg (1.1 mmol, 1.1 equiv.) phenylboronic acid were mixed with 3 mL H_2O/EtOH (1:1, v/v) and heated to 50 °C (see Figure 9B1). After 5 min, when the temperature was achieved, 1.5 mg ($3/3.2 \times 10^{-3}$ mmol Pd, 0.002 equiv.) of catalysts A (**VII**) or B (**XII**), respectively, was added to the solution. The reaction was monitored by HPLC until iodobenzene was completely converted.

2.4.12. Leaching Tests

For analysis of the leaching properties of the catalysts, both model reactions were performed as described before. After the reactions were finished, the catalysts were separated by filtration. The remaining solution of model reaction 1 was heated to 400 °C for 4 h, and 10 mL of aqua regia was added to the residue under stirring for 24 h at 80 °C. The suspension was filtered again and diluted with deionized water to obtain a solution of 20 mL. For model reaction 2, the solvent from the remaining solution was removed under reduced pressure. The resulting residue was dissolved in 5 mL aqua regia and diluted with deionized water to obtain a solution of 20 mL. The Pd content of the solutions was analyzed by the AZBA company employing ICP-MS according to DIN EN ISO 17294-2:2017-01.

3. Results and Discussion

3.1. Synthesis of Catalysts A and B

The synthesis steps to obtain catalyst A (**VII**) and catalyst B (**XII**) are shown in Schemes 2 and 3, respectively. The synthesis protocol of the silica carrier material for both catalysts is based

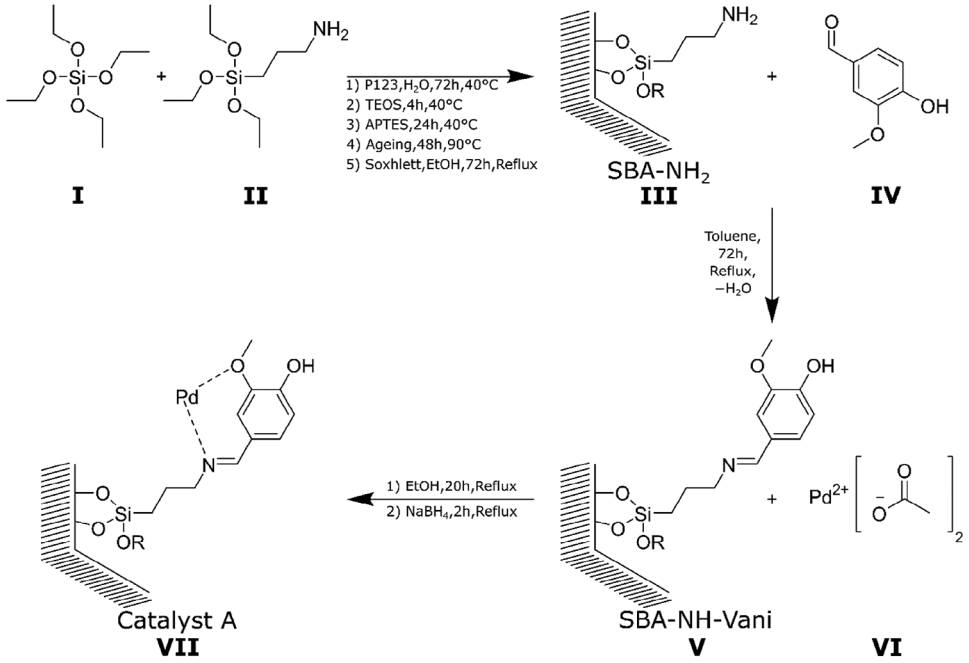

Scheme 2. Synthesis steps to obtain catalyst A (**VII**).

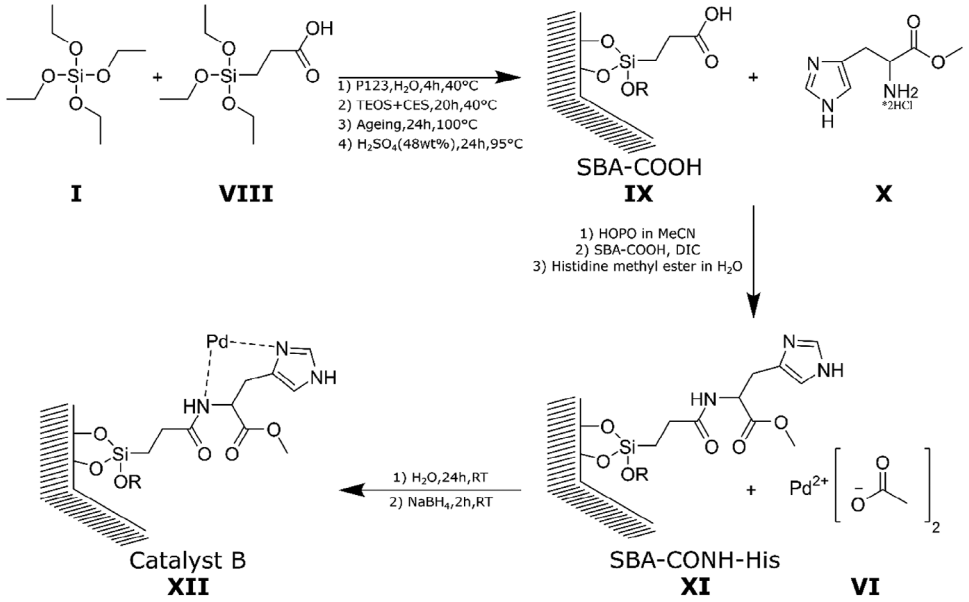

Scheme 3. Synthesis steps to obtain catalyst B (**XII**).

on the co-condensation of TEOS (**I**) with an appropriate silicon-based linker system to achieve a uniform distribution of the linker molecules on the surface. For preparation of catalyst A (**VII**), the APTES linker (**II**) containing an amine head group is used to prepare the modified silica material (**III**), which enables to attach vanillin (**IV**) through imine bond formation between the aldehyde group of the vanillin (**IV**) and the amine group of the linker (**III**). This results in the modified material SBA-NH-Vani (**V**). To achieve a high yield of SBA-NH-Vani (**V**), it is necessary to use water-free solvent and to separate the nascent water with a Dean–Stark apparatus to shift the equilibrium to the product side. The coordination of the Pd(II) acetate (**VI**) is then feasible either via the nitrogen of the imine bond and/or the oxygen of the methoxy group of the vanillin moiety. In the final step, the Pd(II) is reduced with $NaBH_4$ to Pd(0), resulting in catalyst A (**VII**). This step is assumed to improve the catalytic performance in the cross-coupling reactions.[2]

For preparation of catalyst B (**XII**), the CES linker (**VIII**) containing a carboxyl head group is used to prepare the modified silica material (**IX**), which enables the attachment of histidine methyl ester (**X**) via an amide bond. The amide bond is implemented through solid-phase peptide synthesis (SPPS).[79] There-

Table 1. Mass percentages and loadings of nitrogen, carbon, palladium, APTES, and vanillin of the individual synthesis steps of catalyst A (**VII**) calculated by EA and ICP-OES.

Sample	N Content (wt%) | (mmol g^{-1})	C Content	NCH | SiO Content (wt%)	Loading (mmol g^{-1})
SBA-NH_2	2.8 | 2.0	10.5 | 08.8	17.2 | 82.8	2.0[a]
SBA-NH-Vani	2.3 | 1.6	19.8 | 16.5	25.8 | 74.2	1.0[b]
Catalyst A	1.9 | 1.4	13.9 | 11.5	18.8 | 81.2[d]	2.1[c]

[a] APTES loading calculated from nitrogen content.
[b] Vanillin loading calculated from carbon content.
[c] Pd loading determined with ICP-OES.
[d] SiO and Pd content.

fore, the carboxylic group of the histidine needs to be protected through esterification to prevent intermolecular amide formation or dimerization. Besides, the hydrochloric acid salt of the histidine methyl ester is soluble in water and not in solvents for SPPS. The presence of water causes the active ester species of the carboxylic acid with DIC to react to a urea side product instead of the desired amide bond. To prevent this side reaction, the active ester species with DIC is transferred to a water-stable active ester intermediate with 1-HOPO. It is not necessary to hydrolyze the methyl ester acting as a protection group in SBA-CONH-His (**XI**) since it does not interfere with further functionalization. The coordination of Pd(II) acetate (**VI**) is then feasible via the nitrogen atoms from the amide and/or from the imidazole. Subsequently, the coordinated Pd(II) is reduced by $NaBH_4$ to Pd(0).

3.2. Characterization of Catalyst A

3.2.1. Quantification of APTES and Vanillin Content by EA and TGA, and Palladium Content by ICP-OES of Catalyst A (VII)

To investigate the APTES and vanillin content, EA were performed (Table 1). The nitrogen content is the highest for SBA-NH_2 (**III**) and becomes less with each synthesis step performed, while the carbon content reaches its maximum after the attachment of vanillin and is decreased after the coordination and reduction of the palladium. It is, however, higher as for the starting material (**III**). With the introduction of vanillin and palladium, which both do not contain nitrogen, the overall nitrogen content is reduced. Vanillin raises the amount of carbon atoms that is lowered again with the coordination of palladium. Thus, the overall proportion of carbon becomes higher with vanillin and decreases with the addition of palladium since palladium does not decompose in EA like the SiO_2 network. With the mass percentage of nitrogen from SBA-NH_2 (**III**) and the difference in the carbon content between SBA-NH_2 (**III**) and SBA-NH-Vani (**V**), an APTES loading of 2.0 mmol g^{-1} and a vanillin loading of 1.0 mmol g^{-1} equal to 50% degree of functionalization (for calculation see Supporting Information), respectively, is determined.

Next, the organic content obtained in each synthesis step of catalyst A (**VII**) and its thermal stability were studied by TGA. The graphs (Figure S1A) and calculations (Table S1) are presented in the Supporting Information. Catalyst A (**VII**) starts to decompose at approximately 350 °C, making it suitable for reactions up to this temperature. The determined organic and inorganic contents are in good agreement with the results from EA, and a similar loading for vanillin is calculated (see discussion in the Supporting Information). Finally, the palladium mass percentage was determined with ICP-OES to be 21.9%, resulting in a loading of 2.1 mmol g^{-1}. The higher loading of palladium compared to attached vanillin suggests that (i) APTES also coordinates the palladium, (ii) palladium is present as a cluster, and (iii) palladium is adsorbed on the surface or a combination of these three scenarios.

3.2.2. SEM and XPS Analysis of the Synthesis Steps of Catalyst A (VII)

SEM and XPS analyses were performed to investigate the morphology, elemental composition on the surface, and the oxidation state of the palladium in catalyst A (**VII**). Furthermore, backscattered electron (BSE) images as well as a Pd elemental map overlaid with the BSE image were recorded to obtain information on the distribution of Pd. Figure 1A1,A2 shows the SEM images of SBA-NH_2 (**III**) and catalyst A (**VII**), respectively. The morphology of the starting material SBA-NH_2 (**III**) is an agglomerate of rod-like-shaped, uniform particles, which is preserved after functionalization with vanillin, coordination, and reduction of the palladium in the final synthesis step of catalyst A (**VII**). Additionally, the BSE images as well as Pd elemental map were analyzed to investigate the distribution of the palladium in the synthesized catalyst (Figure 2). The BSE image (Figure 2A1) shows a higher magnification of catalyst A (**VII**) compared to Figure 1A2. No significant contrast differences are observed, indicating a homogeneous surface composition. To verify if palladium is on the surface of the material, the BSE image was combined with the Pd elemental map. Figure 2A2 clearly shows a homogeneous distribution of palladium on the surface of the carrier material. Additionally, brighter spots are observed when the magnification is reduced (Figure 2A3) indicating agglomerates/clusters of elements with medium to higher order numbers. These brighter spots contain a higher amount of palladium, as confirmed by comparison of the energy-dispersive X-ray (EDX) spectroscopy spectra of a bright spot to a darker spot (see Supporting Information, Figure S2).

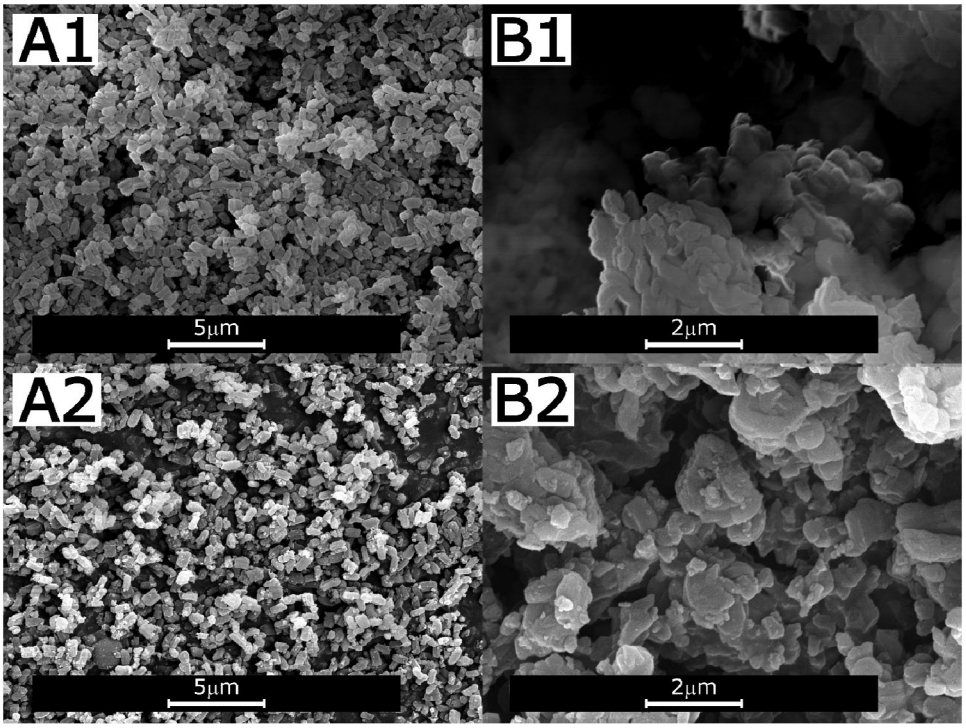

Figure 1. SEM images of SBA-NH_2 (**III**, A1), catalyst A (**VII**, A2), SBA-COOH (**IX**, B1), and catalyst B (**XII**, B2).

The XPS survey spectrum (see Supporting Information, Figure S3) reveals the elemental composition of the surface of the catalyst, which consists of oxygen, carbon, nitrogen, silicon, and palladium, while hydrogen is not detectable. The detailed XPS spectrum of catalyst A (**VII**) in Figure 3A can be deconvoluted into four double peaks, representing four different binding states of palladium. In addition, an artificial double peak is observed due to positive sample charge accumulation known as charging.[80] The first signal pair at 334.9 and 340.1 eV is attributed to bulk-like palladium at the zero state.[81–84] The signal pair at 335.5 and 340.8 eV originates from Pd(0) that is slightly shifted compared to the bulk-like palladium. The higher binding energy is caused by interaction with nitrogen, most probably due to a coordination bond.[81,82,84] The signal pair at 336.7 and 341.8 eV belongs to Pd(0) interacting with oxygen.[81,82] This indicates a coordination bond between the oxygen of the vanillin and palladium. Finally, the signal pair at 338.8 and 344.0 eV is caused by the precursor $Pd(OAc)_2$ that interacts with the support material without being reduced in the last synthesis reaction step. The deconvoluted Pd peak leads to relative areas (in %) of 42.8/31.1/15.0/10.9 for Pd(0)/Pd-N/Pd-O/$Pd(OAc)_2$*. This indicates that 89.1% of the palladium on the support is successfully reduced to Pd(0), and about half of it (42.8%) seems to be in a bulk-like structure.

3.2.3. Gas Adsorption Analysis of the Synthesis Steps of Catalyst A (VII)

The pore structure and pore parameters (pore volume and averaged pore diameter) obtained in each synthesis step have been investigated by nitrogen sorption analysis. SBA-NH_2 (**III**) and SBA-NH-Vani (**V**) show a type IV adsorption–desorption isotherm (Figure 4A) that is characteristic for open mesopores typical for SBA-15.[85] Both samples show a symmetrical hysteresis of type H1 at 0.6–0.75 p/p^0 that indicates a narrow, uniform pore-size distribution[85] and verifies that the pore parameters are preserved after the functionalization with vanillin. Catalyst A (**VII**) displays a similar absorption branch as samples **III** and **V**, but the desorption branch is broadened from 0.5 to 0.75 p/p^0 and appears to have two desorption steps, a shallow one near 0.6 p/p^0 and a sharp one near 0.48 p/p^0. The quantitative analysis of the gas adsorption isotherms in Figure 4A is summarized in Table S3. The specific surface area (BET) is obtained from the linear range at low p/p^0 values from the adsorption isotherms in Figure 4A and results in an expected decrease from SBA-NH_2 (**III**) to SBA-NH-Vani (**V**) but an unexpected small increase to catalyst A (**VII**), as can also be seen from the slightly higher V_{abs}-values in Figure 4A in this region. However, as can be seen in Table S5, repeated syntheses with two sets of SBA-NH-Vani (**V**) and $Pd(OAc)_2$ (**VI**) starting materials show that this outcome is not repeatable; that is, the specific surface area varies with the batch. A plausible explanation is that Pd forms clusters to varying extents on the surface of the support material. Thus, there are two competing effects from the immobilization of Pd onto the functionalized pore surface, namely, a reduction of the pore diameter (and pore volume, as observed in Table S3), which reduces the specific surface area, and the formation of Pd clusters on the surface, which increases the surface area. The formation of the Pd clusters may also explain the appearance of the two steps in the desorption branch of the isotherm in Figure 4A. Interestingly, the pore size distribution obtained from NLDFT analysis in Figure S5A does not appear to capture this differing

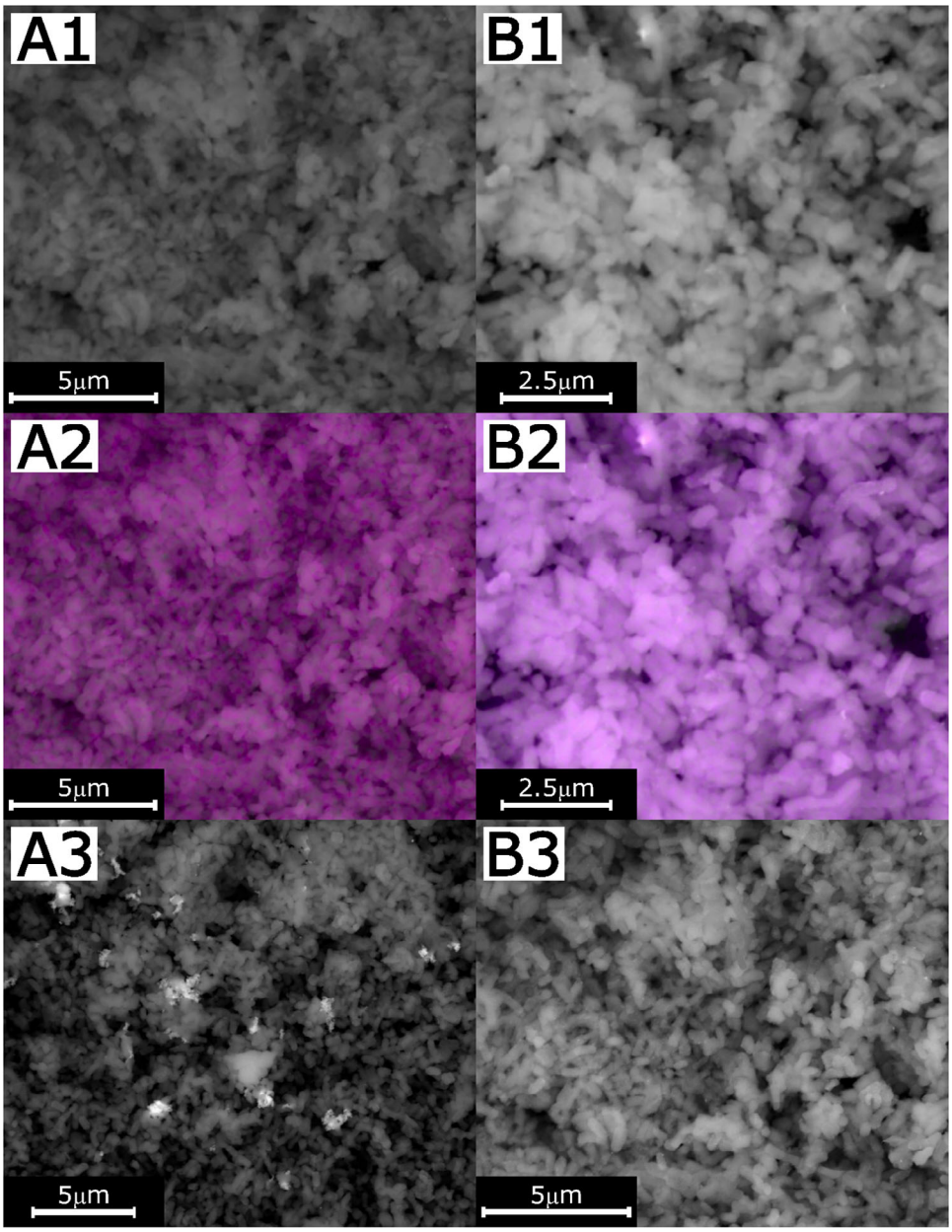

Figure 2. BSE images of catalyst A (**VII**, A1+3) and catalyst B (**XII**, B1+3) with different magnification, and Pd elemental maps overlaid with BSE images for catalyst A (**VII**, A2) and catalyst B (**XII**, B2).

desorption branch shape, while the pore distribution obtained from BJH analysis in Figure S6A is distinctly different from the pore distributions obtained from SBA-NH_2 (**III**) and SBA-NH-Vani (**V**). Specifically, a strong, sharp peak at 4 nm is visible, which may correspond to the sharp desorption step near 0.48 p/p^0, and a weak, broad peak near 5.5 nm, which may correspond to the shallow desorption step near 0.6 p/p^0. Consequently, the pore diameter from BJH analysis in Table S3 drops from 5.7 nm to 4.5 nm upon Pd immobilization, while the corresponding pore diameters obtained from NLDFT stay constant at 7.3 nm. Further elaboration of the reliability of analysis methods by NLDFT and BJH is beyond the scope of this report. We remark that, as pointed out before,[86] BJH analysis tends to underestimate pore diameters,[87,88] while NLDFT analysis tends to overestimate pore diameters.[88] Hence, Tables S3 and S4 also include the average of the two pore diameter analyses.

3.2.4. Solid-State NMR Analysis of the Synthesis Steps of Catalyst A (VII)

The analytics described so far did not provide information about the chemical constitution of the synthesis products and if the palladium is chemically coordinated or maybe just physically absorbed on the surface. For this purpose, ssNMR is employed that allows to inspect local environments in the materials in each synthesis step and to analyze the binding of palladium.

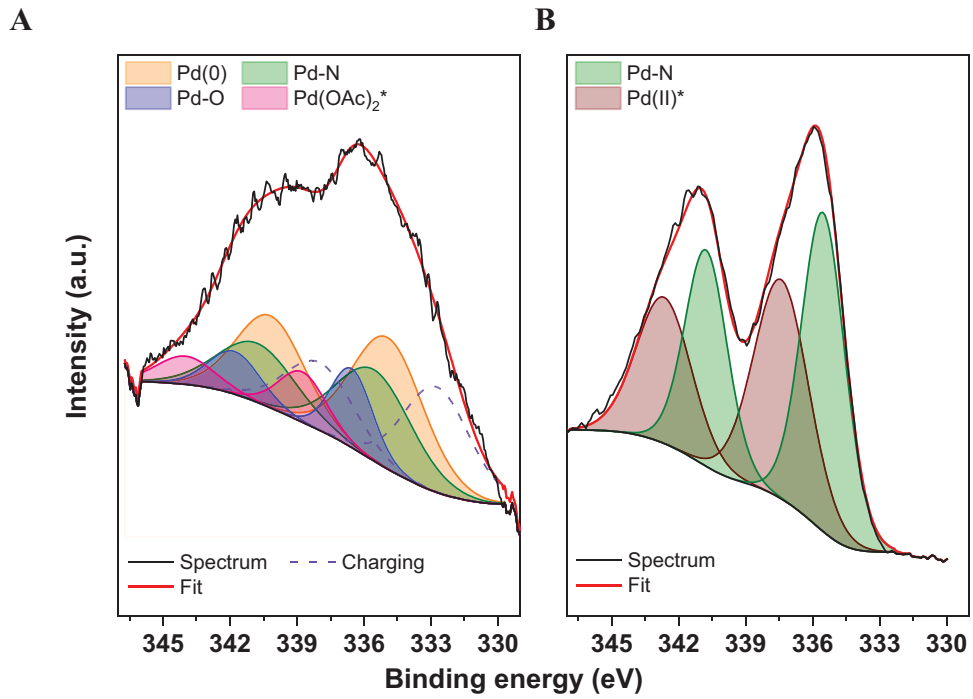

Figure 3. XPS analyses of the binding energies of palladium in the catalysts (catalyst A [**VII**] left and catalyst B [**XII**] right). The black line is the measured spectrum, the red one is the fitting by deconvolution, while the colored lines and areas are fits for the different charge states. Orange is bulk-like Pd(0), green is Pd interacting with nitrogen Pd–N, purple is Pd interacting with oxygen Pd–O, pink is $Pd(OAc)_2$ interacting with the carrier material denoted as $Pd(OAc)_2$*, and brown is a Pd(0) or Pd(II) species interacting with the carrier material denoted as Pd(O/II)*. The dashed line indicates the artificial effect called charging.

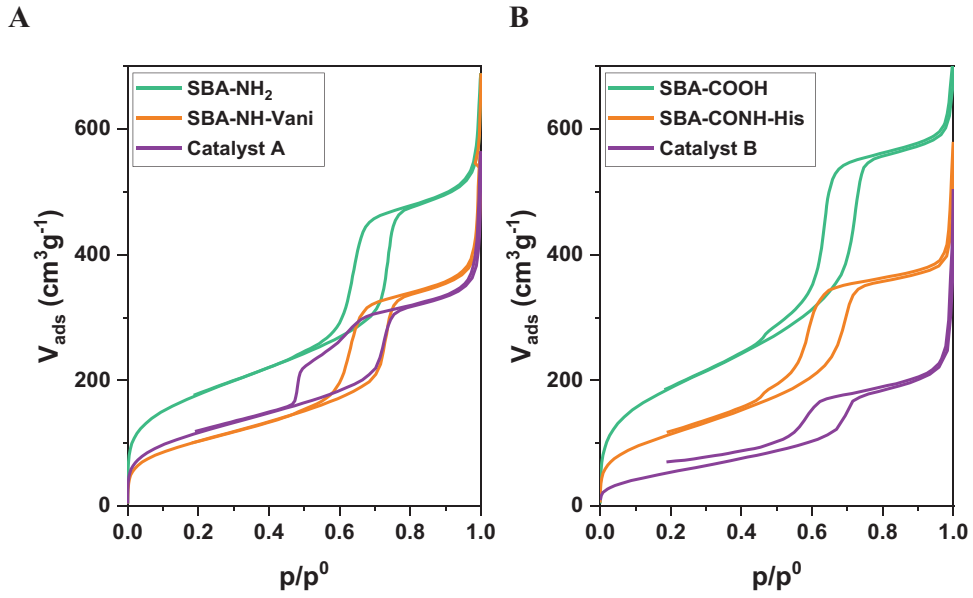

Figure 4. Results from the gas adsorption analysis of each synthesis steps from catalysts A (**VII**) and B (**XII**). $SBA-NH_2$ (**III**) and SBA-COOH (**IX**) are depicted in green, SBA-NH-Vani (**V**) and SBA-CONH-His (**XI**) are illustrated in orange, and the purple isotherms refer to catalysts A (**VII**) and B (**XII**).

$^1H \rightarrow {}^{13}C$ CP MAS ssNMR: In Figure 5, the $^1H \rightarrow {}^{13}C$ CP MAS NMR spectra of $SBA-NH_2$ (**III**) of pure vanillin (**IV**), SBA-NH-Vani (**V**), and catalyst A (**VII**) are shown. In the spectrum of $SBA-NH_2$ (**III**) (Figure 5a), three signals at 9, 21, and 42 ppm are observed that are assigned to the carbons 1, 2, and 3 of the propyl chain of the APTES linker. Additionally, two signals at 17 and 59 ppm (#) are detected that correspond to nonreacted ethoxy groups from the silica precursors TEOS (**I**) and/or APTES (**II**). In the spectrum of pure vanillin (**IV**) (Figure 5b), signals at 57, 105, 115, 128, 132, 148, 154, and 192 ppm are obtained. The signals at 57, 148, 154, and 192 ppm are attributed to the carbons 11, 7, 8, and 4, respectively. The remaining signals are assigned to the other carbons of the

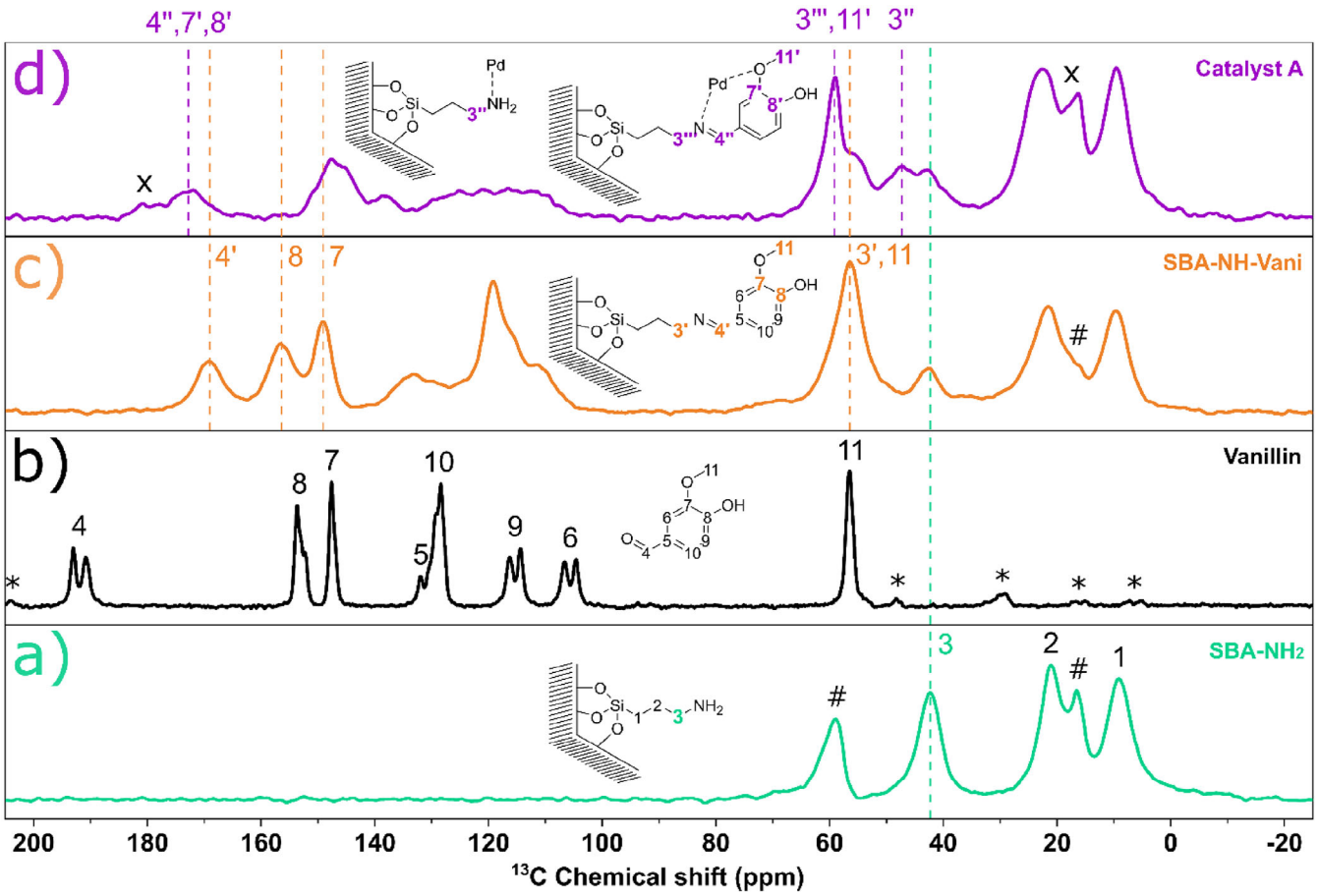

Figure 5. $^{1}H \rightarrow {}^{13}C$ CP MAS spectra of the individual synthesis steps of catalyst A. Depicted in green is the spectrum of SBA-NH_2 (**III**) (a), the black spectrum is pure vanillin (**IV**) (b) as reference, the orange one is SBA-NH-Vani (**V**) (c), and the purple spectrum is catalyst A (**VII**) (d). Note: All spectra were measured at 10 kHz spinning, except the spectrum of SBA-NH_2 (**III**), which was measured at 5 kHz spinning. Signals marked with asterisks (*) are spinning side bands, signals with hash (#) are non-condensed ethoxy groups from the silica precursor, and signals marked with x refer to coordinated $Pd(OAc)_2$ onto the support. Only signals of major interest are labeled with colored numbers. Whenever an already mentioned chemical shift changes its value caused by a functionalization, an apostrophe is added.

benzene ring. After functionalization with vanillin (**IV**) (Figure 5c), the signals of SBA-NH_2 (**III**) are preserved, while the signals of pure vanillin (**IV**) are visible, but with larger line width and slight changes in chemical shift, providing a clear hint for the immobilization. Only the signal at 192 ppm (4) has vanished, while a new signal at 169 ppm (4′) appears. Additionally, the intensity of the signals assigned to nonreacted ethoxy group signals is decreased. The signal at 17 ppm is still visible as a small shoulder of the signal at 21 ppm, and the signal at 59 ppm is overlaid by the signals of the carbon 3′ and 11 with the same chemical shift. The disappearance of the signal at 192 ppm clearly shows that no unreacted vanillin (**IV**) has remained in the material, while the appearance of the signal at 169 ppm indicates the formation of an imine group. These observations suggest the successful binding of the vanillin (**IV**) to the APTES linker via imine. The decrease of the signal intensity of the non-condensed ethoxy groups is most probably caused by their hydrolyzation during the functionalization with vanillin (**IV**).

After immobilization of Pd(II) acetate and reduction to Pd(0) (Figure 5d), the spectral shape in the region between 0 and 70 ppm stays mostly the same except for the appearance of new signals at 16, 47, and 59 ppm and a loss of intensity of the signal at 57 ppm. Since the chemical shifts in the region from 0 to 70 ppm from the previous material (**V**) are still observable, it is assumed that not all surface molecules interact with Pd. The signal at 16 ppm (x) can be attributed to the methyl carbon of coordinated $Pd(OAc)_2$, which is shifted from 23 to 16 ppm (for comparison, see spectrum of neat $Pd(OAc)_2$ (**VI**) in the Supporting Information Figure S7). A change of the chemical shift on a similar order to lower fields was also observed by Liu when the acetate ligands of $Rh_2(OAc)_4$ were replaced by TFA,[89] since such replacement induces a change of the electronic environment at the metal. This indicates that not all $Pd(OAc)_2$ is reduced and that it is coordinated onto the support. The signal at 47 ppm (3″) is caused by free APTES groups that are also able to coordinate Pd, just as the vanillin-functionalized APTES groups coordinate with Pd. The last signal at 59 ppm can be attributed to the carbons 3‴ and 11′ shifted from their original position at 47 ppm (3′ and 11). These new signals indicate different states on the surface after the last reaction step, namely, (i) free APTES groups (3), (ii) vanillin-functionalized APTES groups (3′), and (iii) their partial interaction with Pd (3″, 3‴). To underline this interpre-

tation, SBA-NH_2 (**III**) was treated with $Pd(OAc)_2$ (**VI**) the same way as in the last synthesis step of catalyst A (**VII**). We could observe the same behavior as detected with a new signal of carbon 3 appearing with a slightly higher chemical shift value compared to the original signal (spectrum shown in the Supporting Information, Figure S8). Furthermore, the new signals at 16 and 59 ppm overlay the signals from nonreacted ethoxy groups.

In the region between 100 and 200 ppm, the spectral shape also stays nearly the same while the peaks are broadened, have a lower intensity, and suffer from a loss of resolution. Furthermore, the signals of the carbons 7 and 8 at 148 and 157 ppm vanish, and a new broad signal is detected in the range of 172–180 ppm consisting of four overlapping signals. The first three signals are the shifted signals of carbon 7 to 7′, 8 to 8′, and 4′ to 4″, while the fourth one belongs to $Pd(OAc)_2$. Through coordination of $Pd(OAc)_2$ onto the support as already mentioned above, the original signal is shifted from 190 ppm (see Supporting Information, Figure S7) to 179 ppm. That especially the signals of the carbon atoms 3, 3′, 4′, 7, 8, and 11, which are close to the coordinating atoms, are shifted, while the other signals remain nearly the same underlines that Pd is coordinated by the ligand. The change of chemical shifts is caused by the change of their chemical environment due to the coordination bond.

DNP-enhanced $^1H \rightarrow {}^{15}N$ CP MAS NMR: While ^{13}C chemical shifts are less sensitive to minor changes in electronic environment, ^{15}N chemical shifts are very sensitive to such changes. Therefore, to validate our interpretations of the ^{13}C spectra, we investigated the corresponding ^{15}N spectra. Since ^{15}N in natural abundance has a factor of 50 lower relative sensitivity compared to ^{13}C and is thus in most cases not accessible to solid-state NMR, DNP-enhanced $^1H \rightarrow {}^{15}N$ CP MAS experiments were performed to address nitrogen environments in the materials/catalysts.

The $^1H \rightarrow {}^{15}N$ CP MAS spectrum (NH_4Cl as reference) of SBA-NH_2 (**III**) shows a signal at −5 ppm (Figure 6a, N1), which is assigned to the amine group of the APTES linker that is protonated.[90] After the modification step with vanillin, an additional signal at 140 ppm (Figure 6b, N2) is observed, while the signal at −6 ppm is preserved. The new signal is attributed to a protonated imine nitrogen, which exhibits a large chemical shift change by ~130 ppm to higher field as compared to unprotonated imine nitrogens (270–340 ppm).[91–98] The remaining signal at −6 ppm clearly shows that not all APTES linkers on the silica surface have reacted with vanillin (**IV**). In the $^1H \rightarrow {}^{15}N$ CP MAS spectrum of catalyst A (**VII**) (Figure 6c), the signal at −6 ppm is preserved, while the signal at 140 ppm has vanished, and two new signals at 82 ppm and −54 ppm have appeared. The signal at −54 ppm is assigned to an amine nitrogen (N1′) that coordinates to palladium. In a control experiment, where SBA-NH_2 was treated with $Pd(OAc)_2$ in the same way as the last modification step of catalyst A (**VII**), a comparable change of the chemical shift of the amine group from approx. −5 to approx. −55 ppm is observed (see Supporting Information, Figure S9). Similar trends have also been reported for rhodium catalysts that are coordinated by amine-containing linker groups.[65,99] The disappearance of the signal at 140 ppm clearly shows the coordination of imine to palladium. This hypothesis is underlined by the appearance of a new signal at 82 ppm referring to N2′ that has a chemical shift difference of approximately 60 ppm compared to the signal of the free protonated imine. This chemical shift change is similar to the one obtained for the amine group (−6 ppm, N1) that changes to −54 ppm (N1′) upon coordination to palladium.

3.3. Characterization of Catalyst B

3.3.1. Quantification of CES and Histidine Methyl Ester Content by EA and TGA, and Palladium Content by ICP-OES of Catalyst B (XII)

From EA it is evident that the contents of nitrogen and carbon (Table 2) reach the maximum after binding of the histidine methyl ester (**XI**) and decrease when palladium is immobilized (**XII**). The carboxyl loading is determined from the carbon content (for calculation, see Supporting Information) and amounts to 4.8 mmol g^{-1}. Furthermore, the degree of histidine functionalization is calculated from the nitrogen content since the incorporated amino acid is the only source of nitrogen and amounts to 19%. Taking this value into account, the histidine loading is 0.9 mmol g^{-1}.

Additionally, the thermal stability and the organic content were investigated by TGA (see Supporting Information, Figure S1B and detailed discussion). Catalyst B (**XII**) starts to decompose at approximately 250 °C, making it applicable beneath this temperature. The observed organic and inorganic content are in good agreement with the results from EA with CES and histidine loading (4.8 vs. 5.1 mmol g^{-1} and 0.9 vs. 0.7 mmol g^{-1}), respectively. The palladium weight percentage was determined by ICP-OES to be 21.4 wt%. This value equals a palladium loading of 2.0 mmol g^{-1}.

3.3.2. SEM and XPS Analysis of the Synthesis Steps of Catalyst B (XII)

Figure 1B1,B2 shows the SEM images of SBA-COOH (**IX**) and catalyst B (**XII**), respectively. The image of the starting material **IX** depicts particles with plate-like structure that agglomerate to bigger clusters, an appearance that does not change in the image of **XII**. The BSE images obtained at different magnification (Figure 2B1,B3) exhibit no significant difference in contrasts, which indicates a homogeneous surface composition. Furthermore, the Pd element map overlaid with the BSE image (Figure 2B2) clearly suggests a homogenous distribution of palladium on the surface of the carrier material. The elemental composition of the surface was determined by XPS (see survey spectrum Figure S4 in the Supporting Information). The expanded palladium signal (Figure 3B) suggests two palladium species in the catalyst. The first signal pair at 335.5 and 340.8 eV is caused by Pd(0) that interacts with nitrogen, most probably in a Pd(0)–N coordination bond[81,82,84] originating from the attached histidine (amide and imidazole moieties). From the literature,

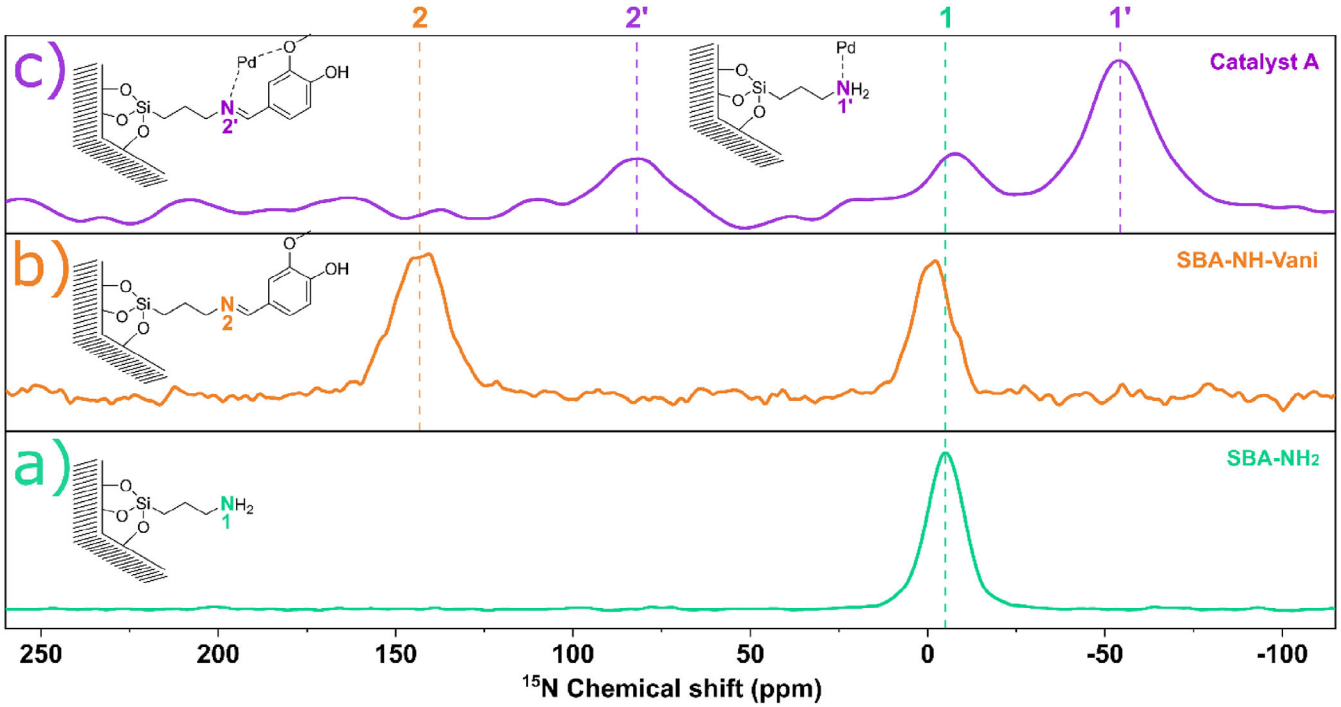

Figure 6. DNP-enhanced $^{1}H \rightarrow {}^{15}N$ CP MAS spectra of the materials obtained in each synthesis step of catalyst A (**VII**). Depicted in green is the spectrum of SBA-NH_2 (**III**, 8 kHz, TOTAPol in D_2O/H_2O) (a), the orange one is SBA-NH-Vani (**V**, 8 kHz, AMUPol in DMSO) (b), and the purple spectrum corresponds to catalyst A (**VII**, 10 kHz, AMUPol in DMSO) (c). Only signals of major interest are labeled with colored numbers. Whenever an already mentioned chemical shift changes its value caused by a functionalization, an apostrophe is added.

Table 2. Mass percentages and loadings of nitrogen, carbon, palladium, CES, and histidine for each individual synthesis step of catalyst B (**XII**) calculated by EA and ICP-OES.

Sample	N Content (wt%) | (mmol g^{-1})	C Content	NCH | SiO Content (wt%)	Loading (mmol g^{-1})
SBA-COOH	0 | 0	17.4 | 14.5	20.4 | 79.6	4.8[a)]
SBA-CONH-His	3.7 | 2.6	21.3 | 17.8	28.4 | 71.6	0.9[b)]
Catalyst B	3.1 | 2.2	18.0 | 15.0	24.1 | 75.9[d)]	2.0[c)]

[a)] CES loading calculated from carbon content.
[b)] Histidine loading calculated from nitrogen content.
[c)] Pd loading determined by ICP-OES.
[d)] SiO and Pd content.

two interpretations of the signal pair at 337.4 and 342.7 eV are suitable: (i) the signal at 337.4 eV indicates Pd(0) interacting with a carboxyl moiety as proposed by Xiao et al.,[100] or (ii) the observed signals denote the formation of a Pd(II) hydroxo species by dissolution and reprecipitation or by adsorption of $Pd(OAc)_2$ with the hydrophilic support material.[81,82] Depending on the interpretation of the spectral data, the palladium on the support was either completely reduced to Pd(0) and interacted with oxygen atoms of catalyst B (**XII**) or a side product such as a divalent hydroxo species was formed.

3.3.3. Gas Adsorption Analysis of the Synthesis Steps of Catalyst B (XII)

All samples possess a type IV adsorption–desorption isotherm (Figure 4B), which is characteristic for open mesopores.[85] For catalyst B (**XII**), the desorption branch does not close on the adsorption branch due to small amounts of remaining water or solvent. Furthermore, all materials show the same shape of a type H1 hysteresis that is not completely symmetric. In the range of p/p^0 0.5–0.6, the loop is extended compared to the range p/p^0 0.7–0.75. This indicates that the pore size distribution of the materials is only slightly broadened compared to the narrow pore size distribution typically found in SBA-15. While the values of V_{abs} decrease from SBA-COOH (**IX**) to SBA-CONH-His (**XI**) to catalyst B (**XII**) in Figure 4B, the shape of the isotherm stays the same. This strongly suggests that the pore structure is preserved for each of the three materials. Only the surface area and corresponding pore volume decrease with increasing size of the surface decoration. Specifically, the quantitative analysis of the adsorption isotherms shown in Table S4 and Figures S5B and S6B in the Supporting Information results in a reduction of

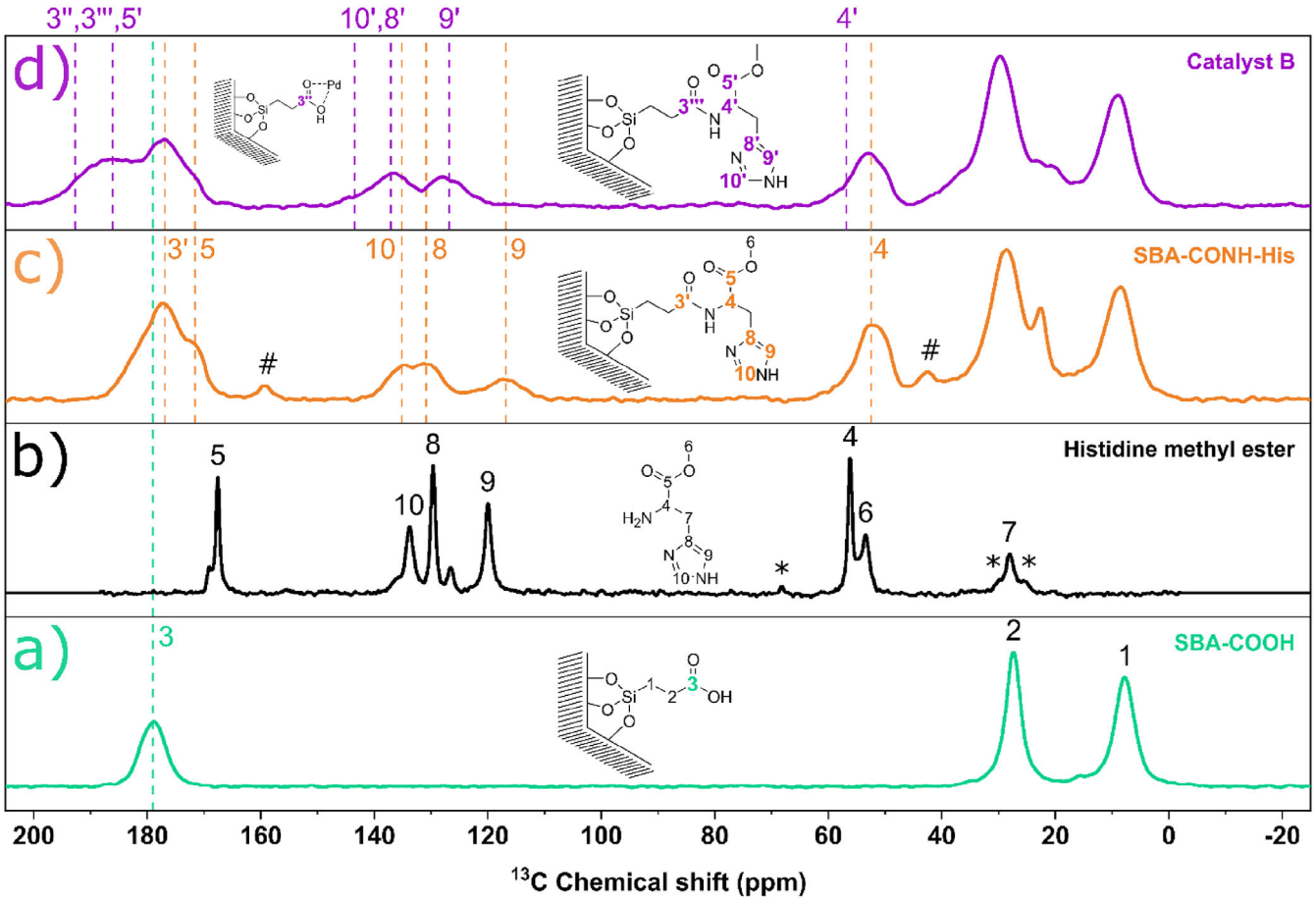

Figure 7. $^{1}H \rightarrow {}^{13}C$ CP MAS spectra of the individual synthesis steps of catalyst B (**XII**). Depicted in green is the spectrum of SBA-COOH (**IX**) (a), the black spectrum is pure histidine methyl ester (**X**) (b) as reference, the orange one is SBA-CONH-His (**XI**) (c), and the purple spectrum is catalyst B (**XII**) (d). Note: All spectra were recorded at 10 kHz spinning. Signals marked with asterisks (*) are spinning side bands, and those with hash (#) are from the side product 1,3-diisopropylurea. Only signals of major interest are labeled with colored numbers. Whenever an already mentioned chemical shift changes its value caused by a functionalization, an apostrophe is added.

specific surface area from 687 to 419 to 208 m^2g^{-1} with a corresponding reduction in volume from 0.9 to 0.59 to 0.34 cm^3g^{-1}. The determined pore diameter also decreases after the binding of the histidine methyl ester (**X**) from 6.5 to 5.8 nm, but it remains unchanged when Pd is coordinated. This is surprising because the addition of Pd should decrease the available space and thus decrease the pore diameter. A possible explanation for this observation is that the Pd is finely dispersed in the sample so that the average pore diameter is immeasurably small affected.

3.3.4. Solid-State NMR Analysis of the Synthesis Steps of Catalyst B (XII)

$^{1}H \rightarrow {}^{13}C$ CP MAS ssNMR: The $^{1}H \rightarrow {}^{13}C$ CP MAS NMR spectra of the materials obtained in each reaction step as well as of pure histidine methyl ester (**X**) as reference, are shown in Figure 7. The spectrum of SBA-COOH (**IX**) (Figure 7a) displays signals at 8, 27, and 179 ppm that are clearly assigned to the carbon atoms 1, 2, and 3 of the CES-linker. In the spectrum of histidine methyl ester (**X**) (Figure 7b), signals at 28, 54, 56, 120, 130, 134, and 168 ppm are observable. The signals at 120, 130, and 134 ppm belong to the carbons 8–10 of the imidazole moiety; the signal at 168 ppm originates from carbon 5 of the ester moiety, the signals at 54 and 56 ppm are attributed to carbons 6 and 4, respectively, and the signal at 28 ppm is assigned to carbon 7. After binding the histidine methyl ester (**X**) to the functionalized silica (**XI**, Figure 7c), all signals referring to the histidine methyl ester (**X**) are broadened, and small changes in the chemical shift are observed, which confirms the presence of interactions of the histidine with the carrier material. Additionally, a broad signal from 171 to 180 ppm has appeared in the spectrum consisting of overlapping signals that are attributed to carbon 3 of free carboxyl linker, carbon 5 of the ester moiety of the histidine methyl ester, and carbon 3′ of the newly formed amide moiety between the linker and the histidine methyl ester. The appearance of the amide carbon signal proves the successful attachment of the histidine methyl ester (**X**) to SBA-COOH (**IX**), while the remaining signal at 179 ppm assigned to carbon 3 of the CES-linker shows that not all carboxyl groups of SBA-COOH (**IX**) have reacted with the histidine methyl ester (**X**). Besides, signals at 23, 43, and 159 ppm with low intensity have appeared, which most probably refer to impurities of the side product 1,3-diisopropylurea.[101]

In the spectrum of catalyst B (**XII**) (Figure 7d), in the range of 0–60 ppm, the signals at 28 and 43 ppm have vanished, while a

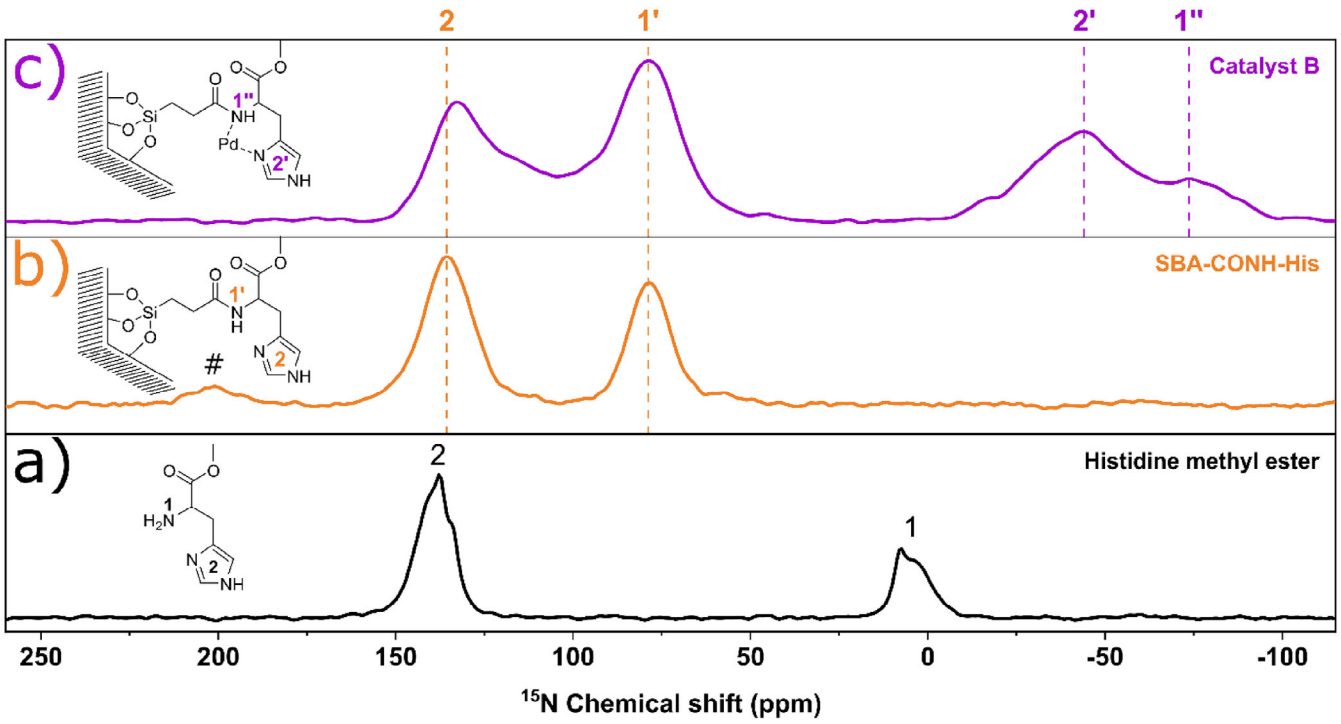

Figure 8. ^{15}N CP MAS DNP spectra of the individual synthesis steps of catalyst B (**XII**). Depicted in black is the spectrum of the pure histidine methyl ester (**X**), the orange one is SBA-CONH-His (**XI**), and the purple spectrum is catalyst B (**XII**). Note: All samples were prepared using an AMUPol in DMSO solution. Spectra of **X** and **XI** were recorded at 8 kHz spinning, while the spectrum of **XII** was recorded at 10 kHz spinning. The Signal marked with hash (#) is from the side product 1,3-diisopropylurea. Only signals of major interest are labeled with colored numbers. Whenever an already mentioned chemical shift changes its value caused by a functionalization, an apostrophe is added.

new signal at 55 ppm appears. The signals of SBA-CONH-His (**XI**) are preserved, meaning that not all surface functional groups interact with Pd. The disappeared signals at 23 and 43 ppm belong to 1,3-diisopropylurea. This suggests that the side product from the synthesis of SBA-CONH-His (**XI**) was washed out during the last synthesis step. The new signal at 55 ppm originates from carbon 4′ that has shifted from 50 ppm (carbon 4) due to interaction of the neighboring atoms with Pd. In the region of 110–200 ppm, further changes to the spectrum can be observed. The signals at 116, 130, 134, and 159 ppm have vanished, and new signals at 128, 137, and 180–190 ppm appear. The signal at 128 ppm belongs to carbon 9′ that is shifted from 116 ppm (carbon 9). The signal at 137 ppm is attributed to the carbons 8′ and 10′ that now overlap and were shifted from 130 ppm (carbon 8) and 134 ppm (carbon 10). The vanishing signal at 159 ppm originates from the side product 1,3-diisopropylurea mentioned earlier, which underlines our hypothesis that it was washed out. The broad signal from 180 to 190 ppm can be contributed to the overlapping signals of carbon 3″, 3″, and 5′. This observation suggests that besides the nitrogen atoms, the oxygen atoms of the amide and carboxyl moieties are also able to coordinate Pd, which leads to the low field shift of the carbons 3, 3′, and 5 from 170–178 to 180–190 ppm. As already observed in the ^{13}C spectrum of catalyst A (**VII**), all carbons in close vicinity to the coordinating atoms are shifted, while the other signals remain the same. We note that such significant spectral changes to the mentioned signals of the ^{13}C spectrum would not be expected for physiosorbed Pd but are consistent with chemisorbed palladium. To validate the hypothesis that palladium is chemisorbed via coordination bonds with histidine methyl ester, DNP-enhanced ^{1}H → ^{15}N CP MAS ssNMR was employed.

DNP-enhanced ^{1}H → ^{15}N CP MAS NMR: The DNP-enhanced ^{1}H → ^{15}N CP MAS NMR spectrum of pure histidine methyl ester (**X**) (Figure 8a) displays signal groups at 8 and 138 ppm that are assigned to the nitrogen atoms in amine (N1) and in imidazole (N2), respectively. Usually, the nitrogen atoms in the imidazole should show two different signals.[102,103] Since the histidine methyl ester was used as dihydrochloride salt, the nitrogen atoms are protonated and therefore are almost chemically equivalent, resulting in the same chemical shift.[104] After reaction of the histidine methyl ester (**X**) with SBA-COOH (**IX**), forming SBA-CONH-His (**XI**) (Figure 8b), the signal at 8 ppm has completely vanished, and two new signals at 79 and 202 ppm appear. These new signals are attributed to the nitrogen in the formed amide group (N1′) and the nitrogen in the side product 1,3-diisopropylurea (#), respectively. The signal at 138 ppm assigned to the nitrogen atoms of the imidazole ring (N2) is preserved. Even though the histidine methyl ester is not in the dihydrochloride salt form anymore, it is still in its protonated state like before. This is due to the acidic environment of the silica surface, which also led to the protonation of the imine in catalyst A (**VII**). The disappearance of the signal at 8 ppm (amine nitrogen) and the appearance of the signal at 79 ppm (amide nitrogen) clearly demonstrate the successful covalent binding of

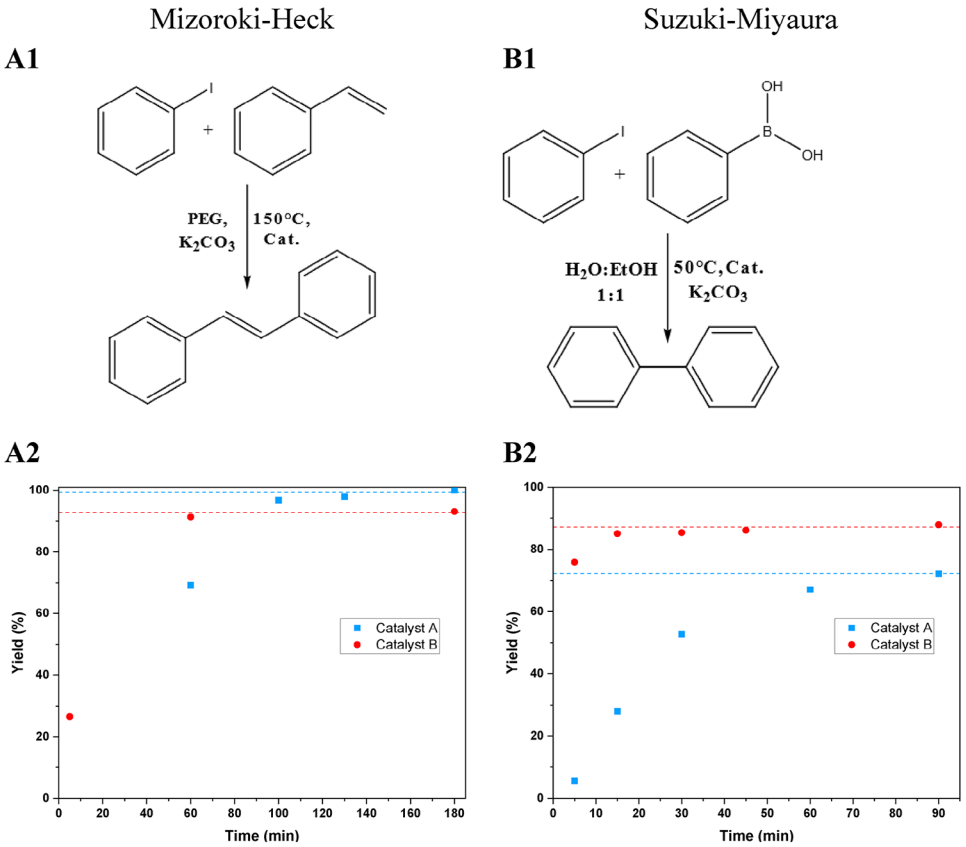

Figure 9. C–C coupling of iodobenzene and styrene in the presence of catalyst A (**VII**) or B (**XII**) and K_2CO_3 in PEG-400 at 150 °C as a model for the Mizoroki–Heck cross-coupling reaction (A1). Yield of *trans*-stilbene obtained at different times during the Mizoroki–Heck reaction with both catalysts (catalyst A (**VII**), blue; catalyst B (**XII**) red) (A2). C–C coupling of iodobenzene and phenylboronic acid in the presence of catalyst A (**VII**) or B (**XII**) and K_2CO_3 in H_2O/EtOH (1:1) at 50 °C as a model for the Suzuki–Miyaura cross-coupling reaction (B1). Yield of biphenyl obtained at different times during the Suzuki–Miyaura reaction with both catalysts (catalyst A (**VII**), blue; catalyst B (**XII**), red) (B2). The dotted lines serve as a visual aid for the maximum yield.

the histidine methyl ester (**X**) to SBA-COOH (**IX**) and underline our interpretation of the $^{1}H \rightarrow {}^{13}C$ CP MAS spectra.

The coordination of palladium (Figure 8c) results in a broadening of the signals at 79 ppm (N1′) and 138 ppm (N2) obtained in the spectrum of SBA-CONH-His (**XI**, Figure 8b). Furthermore, two new signals at −44 and −74 ppm have appeared, while the signal at 202 ppm from the side product has vanished. The high-field-shifted signals at −74 and −44 ppm marked in Figure 8c with N1″ and N2′, respectively, most probably originate from the amide and imidazole nitrogen atoms interacting with Pd, while the preserved signals from the prior modification step indicate the presence of non-coordinating histidine molecules.

3.4. Test of the Catalytic Activity of Catalysts A (VII) and B (XII)

To evaluate the performance of catalysts A (**VII**) and B (**XII**), they are tested in the Mizoroki–Heck (Figure 9A1) and Suzuki–Miyaura (Figure 9B1) cross-coupling reactions between styrene with iodobenzene and phenylboronic acid with iodobenzene, respectively. The identification and quantification of the products are done by gas chromatography (GC) for the Mizoroki–Heck, and by high-performance liquid chromatography (HPLC) for the Suzuki–Miyaura reaction.

In Figure 9A2 the yield of *trans*-stilbene in the Mizoroki–Heck cross-coupling reaction is plotted as a function of the reaction time for both catalysts. After 180 min of reaction, 100% and 93% yields are obtained with catalysts A (**VII**) and B (**XII**), respectively. This clearly shows that both heterogeneous catalysts enable the reaction in PEG-400 at 150 °C with excellent performance. Figure 9B2 shows the yield of biphenyl in the Suzuki–Miyaura cross-coupling reaction plotted as a function of the reaction time for both catalysts. After 90 min of reaction, 72% and 88% yields are obtained with catalyst A (**VII**) and B (**XII**), respectively. This demonstrates that both heterogeneous catalysts enable the production of biphenyl in H_2O/EtOH (1:1) even at moderate temperatures of 50 °C with very good performance.

Although both catalysts enable significant conversion in the Mizoroki–Heck and the Suzuki–Miyaura cross-coupling reactions, they differ in their efficiency. While catalyst A (**VII**) preferably catalyzes the Mizoroki–Heck reaction at 150 °C, catalyst B (**XII**) preferably catalyzes the Suzuki–Miyaura at 50 °C. In addition to the catalytic tests, exemplary leaching tests were performed, analyzing the Pd content in the filtrate solution after reaction. Leaching of Pd in the range of 2 up to 15% (see Supporting Information, Table S6) from the catalysts was observed that may affect the catalytic activity and stability of the two catalysts. A more detailed discussion is provided in the next section.

3.5. Comparison of Catalyst A (VII) and Catalyst B (XII)

Having presented the characterization of each catalyst separately, this section compares the findings for catalyst A (**VII**) and catalyst B (**XII**) and further interprets any observed differences. The successful synthesis of each catalyst was confirmed through ssNMR spectral characterization of precursors, intermediates, and final catalyst products. $^{1}H \rightarrow {}^{13}C$ CP MAS NMR spectra from the two final catalysts show changes in chemical shifts of those signals that represent the carbon atoms in close vicinity to the functional groups that are interacting with the palladium, likely via a coordination bond. In addition, new spectral features were observed in both $^{1}H \rightarrow {}^{13}C$ CP MAS NMR and DNP-enhanced $^{1}H \rightarrow {}^{15}N$ CP MAS NMR of the final catalyst compound. For example, the carbon atom next to the amine linker (signal 3–3″ in Figure 5) for catalyst A (**VII**) and the carbon of the carboxyl group (signal 3–3″ in Figure 7) for catalyst B (**XII**) display a new spectral signal. Furthermore, the NMR spectral data showed that not all linker molecules reacted with vanillin or histidine methyl ester and that some of the Pd coordinated with these unreacted linker molecules as well. The quantification of loadings of amine/carboxyl (**III, IX**), vanillin/methyl histidine (**V, XI**), and palladium resulted in 2.0, 1.0, and 2.1 mmol g^{-1} for catalyst A (**VII**) and 4.8–5.1, 0.9, and 2.0 mmol g^{-1} for catalyst B (**XII**), respectively. Although catalyst B (**XII**) showed a factor of 2.5 higher loading of carboxyl (**IX**) compared to amine (**III**) groups, the amount of histidine methyl ester (**XI**) was similar compared to vanillin (**V**) in catalyst A (**VII**). From TGA analyses, catalyst A (**VII**) showed a higher thermal stability compared to catalyst B (**XII**), as catalyst A (**VII**) started to degrade at 350 °C, while catalyst B (**XII**) started to degrade at 250 °C. From combined results of the thermal and gas adsorption analyses, the number of CES residues per surface area was found to be 4.2 nm^{-2} for catalyst B (**XII**), which is higher than the determined 1.9 nm^{-2} APTES residues for catalyst A (**VII**). The values for the functionalization and Pd were found to be nearly the same between the two catalysts, with 1.0 nm^{-2} (vanillin) and 2.0 nm^{-2} (Pd) for catalyst A (**VII**) and 0.8 nm^{-2} (histidine methyl ester) and 2.0 nm^{-2} (Pd) for catalyst B (**XII**), respectively.

The XPS analyses for both catalysts showed the expected signals of Pd interacting with the intended amine and oxygen groups of the corresponding support material. Additionally, signals for bulk-like Pd(0) (~43%) and $Pd(OAc)_2$ (~11%) were observed for catalyst A (**VII**), suggesting clustering of the palladium in the zero-state and that non-reduced palladium is anchored on the carrier material. The assumption of clustering is supported by the results from the thermal, gas adsorption, and SEM-EDX analyses as summarized further below. In the thermal analysis, a loading of Pd equal to the amine was observed. This indicates that in addition to the vanillin-functionalized groups, the amine is coordinating Pd as well. This interpretation is further underlined by the DNP-enhanced $^{1}H \rightarrow {}^{15}N$ CP MAS spectra, which display a new shifted signal for the amines. However, signals from pristine amine were also observed, showing that Pd is only partially coordinated, which implies the presence of excess Pd and is consistent with the presence of Pd clusters. The presence of clusters is also supported by the area ratios of the different deconvoluted XPS signals, which include one signal consistent with bulk-like Pd. Furthermore, it is consistent with the unexpected increase of the specific surface area after the reaction step with $Pd(OAc)_2$. Specifically, the presence of Pd clusters on the surface produces local bulged surface morphologies that increase the surface area. Additionally, ^{13}C NMR signals of $Pd(OAc)_2$ were observed to be shifted from pristine $Pd(OAc)_2$, which supports that not all coordinated precursor was reduced to Pd(0). Finally, the Pd elemental maps overlaid with the BSE images show a homogenous distribution of palladium on the surface of the carrier material for both catalysts. At reduced magnification, however, spots with higher amounts of palladium are visible in the BSE image combined with EDX only for catalyst A (**VII**). This clearly underlines the assumption of agglomerated/clustered palladium present in catalyst A (**VII**), which are located at the surface.

The XPS analysis of catalyst B (**XII**) showed a signal for which two possible interpretations are suggested in the literature, either the presence of a Pd(II) hydroxo species[81,82] or the presence of Pd(0) interacting with oxygen.[100] The $^{1}H \rightarrow {}^{13}C$ CP MAS NMR spectra revealed that the latter is the case because the observed shifted signals from the carboxyl groups strongly indicate an interaction of Pd with oxygen.

The gas adsorption isotherms for both support materials (**III, IX**) displayed characteristics for SBA-15 that are preserved during the syntheses while the pore volume and diameter decreased during the synthesis for each catalyst. However, for catalyst A (**VII**), there were some strongly differentiating features in the gas adsorption isotherm. The specific surface area was found to increase, and the desorption branch was of a broadened shape with a small step at 0.48 p/p^0 in addition to the steep step at 0.6 p/p^0 that was observed also in the other materials. These specific features resulted in a non-uniform pore size distribution in the BJH analysis consistent with a two-step desorption process. Additionally, the decrease of the pore diameter from ~5.5 nm to ~3.9 nm was unexpectedly high. Typically, the decrease of the pore diameter was in the range of $\leq$1 nm, which in fact was observed during the attachment step of vanillin and methyl histidine. The higher diameter reduction therefore also indicates the presence of clustered Pd as already mentioned above. The amount of Pd clustering appeared to depend on batch-to-batch variations of the palladium precursor $Pd(OAc)_2$ based on repeated syntheses and analyses of catalyst A (**VII**). Specifically, there was a reproducible increase of the surface area after the coordination of palladium with one batch of $Pd(OAc)_2$, but not with a different batch.

With respect to catalyst B (**VII**), the specific surface area decreased as expected, but the results of the gas adsorption of catalyst B (**VII**) showed an unchanged pore diameter after the last reaction step. In contrast to catalyst A (**VII**), the Pd in catalyst B (**XII**) seems to be finely dispersed and the change of the diameter is not measurable. This assumption is further underlined by the BSE images combined with EDX.

In the catalytical tests, both catalysts show different performances. In the model Heck reaction, catalyst A (**VII**) reaches a yield of the desired product of nearly 100% while catalyst B (**XII**) achieves a maximum of ~93% but in a shorter reaction time. In the Suzuki model reaction, catalyst B (**XII**) achieves a higher

maximum yield of ~88% and quicker (~15 min) than catalyst A (**VII**) with a maximum yield of ~72% after 90 min. The different catalytic performances of the catalysts may be caused by the different morphology they inherit. The morphology determined by SEM is a rod-like structure for catalyst A (**VII**) and a plate-like one for catalyst B (**XII**) that remains unchanged throughout the synthesis. These differences in morphology may be a reason for the different efficiency of the catalysts in the two-model cross-coupling reactions. Besides, both catalysts have similar pore properties and loadings of palladium, which suggests that they most likely have a small influence on their catalytic performance and are not the cause of the differences. Another aspect that may lead to different catalytic performance could be the dispersion of Pd. For catalyst A (**VII**), we have dispersed and mostly agglomerated/clustered Pd, while for catalyst B (**XII**), it seems to be finely dispersed. This could lead to different interaction behaviors of the substrates and solvents during the catalysis. During the catalysis, leaching from 2% up to 15% was observed. More precisely, 13% and 2% for catalyst A (**VII**) and 14% and 15% for catalyst B (**XII**) in the Mizoroki–Heck and Suzuki–Miyaura reactions, respectively. This leaching is most probably caused by palladium, which is not only located inside the pores but also on the surface. While the leaching characteristics are nearly identical, the value for catalyst A (**VII**) in the Suzuki–Miyaura reaction is significantly less than for the others. These results indicate that leaching is dependent on (i) the reaction itself, (ii) the used substrates, and (iii) reaction conditions like temperature and solvent, or a combination of them. To analyze this in detail, further experiments are necessary that are beyond the scope of this work.

4. Conclusion

Overall, this study shows how to successfully immobilize Pd onto mesoporous silica material via a straightforward and inexpensive synthesis route in three steps under mostly mild reaction conditions using nontoxic, commercially available chemicals, including natural products as ligands. The structural properties of the support material as well as the intermediates obtained after each synthesis step were monitored by different analytics. The amount of amine/carboxyl groups and vanillin/histidine methyl ester and the thermal stability were determined by TGA and EA, while ICP-OES delivered the amount of palladium of the catalysts. The morphology was investigated by SEM and XPS and confirmed the presence of coordinated palladium in the zero-oxidation state. Gas adsorption analysis was conducted, which indicated the presence of palladium agglomerates/clusters in one of the two catalysts, which was underlined by BSE images combined with EDX. A careful ^{13}C solid-state NMR and DNP-enhanced ^{15}N solid-state NMR spectral analysis was presented, which provided ultimate proof of the successful syntheses of the catalysts. The coordination of the palladium onto the carrier material was shown by combining the NMR spectral results with the results of the other analytics. Good catalytic performance with yields of the products from 88% up to nearly 100% for the important cross-coupling reactions Heck and Suzuki in PEG and H_2O/EtOH (1:1) as green solvents, respectively, were obtained with these new heterogeneous catalysts, which could be further increased by optimization of the reaction conditions. These model catalysts might be attractive for physicochemical investigations to elucidate various effects from, for example, host-guest interactions and solvation dynamics under confinement on the effectiveness of heterogeneous catalysts in general. For such studies, DNP-enhanced solid-state NMR as employed in this study combined with theoretical work such as MD simulations may especially be fruitful, as pointed out in a recent review.[105]

Author Contributions

Till Wissel performed the syntheses, basic characterization, and catalytic tests of the novel catalysts and wrote the manuscript draft. Mark V. Höfler measured and processed the solid-state DNP data. Marcos de Oliveira Jr. supported the solid-state DNP measurements. Martin Brodrecht and Kevin Herr supported the syntheses of the catalysts and adsorption/desorption measurements. Lorenz Rösler supported the catalytic test measurements. Hergen Breitzke and Vytautas Klimavicius performed the standard solid-state NMR investigations. Martin Ebert measured the BSE images in combination with Pd element maps. Markus Hoffmann supported the writing and proofread the manuscript. Gerd Buntkowsky conceptualized and supervised the project and proofread the manuscript. Torsten Gutmann concepted the manuscript and co-supervised the project.

Acknowledgements

This work has been supported by the National Science Foundation (NSF) under grant no. (1953428) and the Deutsche Forschungsgemeinschaft (DFG) under grant Bu-911/24-3. The latter included a Mercator fellowship for M.M.H. The authors thank Mr. Kopp (TU Darmstadt) for XPS measurements and Prof. Hess (TU Darmstadt) for providing measurement time on his Surface Science Laboratories Inc. SSX 100 ESCA spectrometer.

Open access funding enabled and organized by Projekt DEAL.

Conflict of Interests

The authors declare no conflict of interest.

Data Availability Statement

The data that support the findings of this study are available from the corresponding author upon reasonable request.

Keywords: Heterogeneous catalyst · Pd cross-coupling · Polyethylene glycol · SBA-15 · Solid-state DNP NMR

[1] D. Astruc, *Inorg. Chem.* **2007**, *46*, 1884–1894.
[2] A. Biffis, P. Centomo, A. Del Zotto, M. Zecca, *Chem. Rev.* **2018**, *118*, 2249–2295.

[3] M. Gholinejad, Z. Naghshbandi, C. Nájera, *ChemCatChem* **2019**, *11*, 1792–1823.
[4] J. Durand, E. Teuma, M. Gómez, *Eur. J. Inorg. Chem.* **2008**, 3577–3586.
[5] J. A. Glaser, in *Greener Synthesis of Organic Compounds, Drugs and Natural Products* (Ed: A. Nag), CRC Press, Boca Raton, FL **2022**, pp. 151–176.
[6] F. Habeche, M. Hachemaoui, A. Mokhtar, K. Chikh, F. Benali, A. Mekki, F. Zaoui, Z. Cherifi, B. Boukoussa, *J. Inorg. Organomet. Polym. Mater.* **2020**, *30*, 4245–4268.
[7] G. Martínez-Edo, A. Balmori, I. Pontón, A. Del Martí Rio, D. Sánchez-García, *Catalysts* **2018**, *8*, 617.
[8] L. Djakovitch, K. Köhler, J. G. de Vries, in *Nanoparticles and Catalysis* (Ed.: D. Astruc), Wiley-VCH, Weinheim **2007**, pp. 303–348.
[9] A. Rajendran, M. Rajendiran, Z.-F. Yang, H.-X. Fan, T.-Y. Cui, Y.-G. Zhang, W.-Y. Li, *Chem. Rec.* **2020**, *20*, 513–540.
[10] V. Polshettiwar, C. Len, A. Fihri, *Coord. Chem. Rev.* **2009**, *253*, 2599–2626.
[11] P. Veerakumar, P. Thanasekaran, K.-L. Lu, S.-B. Liu, S. Rajagopal, *ACS Sustain. Chem. Eng.* **2017**, *5*, 6357–6376.
[12] J. G. de Vries, *Dalton Trans.* **2006**, *3*, 421–429.
[13] M. A. Andrade, D. R. S. Martins, *Molecules* **2020**, *25*, 5506.
[14] F. Christoffel, T. R. Ward, *Catal. Lett.* **2018**, *148*, 489–511.
[15] R. F. Heck, J. P. Nolley, *J. Org. Chem.* **1972**, *37*, 2320–2322.
[16] S. Baba, E. Negishi, *J. Am. Chem. Soc.* **1976**, *98*, 6729–6731.
[17] N. Miyaura, K. Yamada, A. Suzuki, *Tetrahedron Lett.* **1979**, *20*, 3437–3440.
[18] M. Díaz-Sánchez, D. Díaz-García, S. Prashar, S. Gómez-Ruiz, *Environ. Chem. Lett.* **2019**, *17*, 1585–1602.
[19] E. Turunç, S. Akay, T. Baran, D. Kalderis, T. Tsubota, B. Kayan, *New J. Chem.* **2021**, *45*, 12519–12527.
[20] T. Tamoradi, M. Daraie, M. M. Heravi, *Appl. Organomet. Chem.* **2020**, *34*, e5538.
[21] S. Sharma, U. P. Singh, *Results Chem.* **2021**, *3*, 100189.
[22] M. Binandeh, M. A. Nasseri, A. Allahresani, *Catalysts* **2022**, *12*, 976.
[23] A. R. Hajipour, Z. Khorsandi, *Nanochem. Res.* **2019**, *4*, 132–139.
[24] M. Shariatipour, A. Heydari, *ChemistrySelect* **2021**, *6*, 1107–1117.
[25] K. Köhler, W. Kleist, S. S. Pröckl, *Inorg. Chem.* **2007**, *46*, 1876–1883.
[26] V. Polshettiwar, Á. Molnár, *Tetrahedron* **2007**, *63*, 6949–6976.
[27] S. Mukhopadhyay, G. Rothenberg, A. Joshi, M. Baidossi, Y. Sasson, *Adv. Synth. Catal.* **2002**, *344*, 348–354.
[28] K. Köhler, M. Wagner, L. Djakovitch, *Catal. Today* **2001**, *66*, 105–114.
[29] S. Jagtap, *Catalysts* **2017**, *7*, 267.
[30] M. R. dos Santos, R. Coriolano, M. N. Godoi, A. L. Monteiro, H. C. B. de Oliveira, M. N. Eberlin, B. A. D. Neto, *New J. Chem.* **2014**, *38*, 2958.
[31] J. G. de Vries, *Can. J. Chem.* **2001**, *79*, 1086–1092.
[32] H.-U. Blaser, A. Indolese, F. Naud, U. Nettekoven, A. Schnyder, *Adv. Synth. Catal.* **2004**, *346*, 1583–1598.
[33] M. Pérez-Lorenzo, *J. Phys. Chem. Lett.* **2012**, *3*, 167–174.
[34] I. P. Beletskaya, A. V. Cheprakov, *Chem. Rev.* **2000**, *100*, 3009–3066.
[35] A. F. Littke, G. C. Fu, *Angew. Chem., Int. Ed.* **2002**, *41*, 4176–4211.
[36] L. Rösler, M. V. Höfler, H. Breitzke, T. Wissel, K. Herr, H. Heise, T. Gutmann, G. Buntkowsky, *Cellulose* **2022**, *29*, 6283–6299.
[37] M. Khanmoradi, M. Nikoorazm, A. Ghorbani-Choghamarani, *Catal. Lett.* **2017**, *147*, 1114–1126.
[38] A. R. Hajipour, Z. Khorsandi, *Appl. Organomet. Chem.* **2016**, *30*, 256–261.
[39] A. H. Labulo, B. S. Martincigh, B. Omondi, V. O. Nyamori, *J. Mater. Sci.* **2017**, *52*, 9225–9248.
[40] D. A. Alonso, A. Baeza, R. Chinchilla, C. Gómez, G. Guillena, I. M. Pastor, D. J. Ramón, *Catalysts* **2018**, *8*, 202.
[41] B. W. Glasspoole, J. D. Webb, C. M. Crudden, *J. Catal.* **2009**, *265*, 148–154.
[42] A. Modak, J. Mondal, A. Bhaumik, *Green Chem.* **2012**, *14*, 2840.
[43] Á. Molnár, *Chem. Rev.* **2011**, *111*, 2251–2320.
[44] R. Tao, X. Ma, X. Wei, Y. Jin, L. Qiu, W. Zhang, *J. Mater. Chem. A* **2020**, *8*, 17360–17391.
[45] A. Gniewek, J. Ziolkowski, A. Trzeciak, M. Zawadzki, H. Grabowska, J. Wrzyszcz, *J. Catal.* **2008**, *254*, 121–130.
[46] X. S. Zhao, G. Q. Lu, G. J. Millar, *Ind. Eng. Chem. Res.* **1996**, *35*, 2075–2090.
[47] B. A. de Marco, B. S. Rechelo, E. G. Tótoli, A. C. Kogawa, H. R. N. Salgado, *Saudi Pharma. J.* **2019**, *27*, 1–8.
[48] A. Nag, H. S. Maity, in *Greener Synthesis of Organic Compounds, Drugs and Natural Products* (Ed: A. Nag), CRC Press, Boca Raton **2022**, pp. 1–22.
[49] M. O. Sydnes, *Curr. Green Chem.* **2019**, *6*, 96–104.
[50] D. B. Eremin, V. P. Ananikov, *Coord. Chem. Rev.* **2017**, *346*, 2–19.
[51] L. Shao, B. Zhang, W. Zhang, S. Y. Hong, R. Schlögl, D. S. Su, *Angew. Chem., Int. Ed.* **2013**, *52*, 2114–2117.
[52] K. Motokura, S. Ding, K. Usui, Y. Kong, *ACS Catal.* **2021**, *11*, 11985–12018.
[53] P. Albers, *Chem. Ing. Tech.* **2006**, *78*, 835–849.
[54] F. Blanc, J.-M. Basset, C. Copéret, A. Sinha, Z. J. Tonzetich, R. R. Schrock, X. Solans-Monfort, E. Clot, O. Eisenstein, A. Lesage, L. Emsley, *J. Am. Chem. Soc.* **2008**, *130*, 5886–5900.
[55] F. Blanc, C. Copéret, A. Lesage, L. Emsley, *Chem. Soc. Rev.* **2008**, *37*, 518–526.
[56] C. Copéret, A. Comas-Vives, M. P. Conley, D. P. Estes, A. Fedorov, V. Mougel, H. Nagae, F. Núñez-Zarur, P. A. Zhizhko, *Chem. Rev.* **2016**, *116*, 323–421.
[57] C. Copéret, W. C. Liao, C. P. Gordon, T. C. Ong, *J. Am. Chem. Soc.* **2017**, *139*, 10588–10596.
[58] P. Gao, G. J. Hou, *Magn. Reson. Lett.* **2023**, *3*, 31–42.
[59] D. Grekov, T. Vancompernolle, M. Taoufik, L. Delevoye, R. M. Gauvin, *Chem. Soc. Rev.* **2018**, *47*, 2572–2590.
[60] T. Gutmann, I. Del Rosal, B. Chaudret, R. Poteau, H. H. Limbach, G. Buntkowsky, *ChemPhysChem* **2013**, *14*, 3026–3033.
[61] T. Gutmann, P. B. Groszewicz, G. Buntkowsky in *Annual Reports on NMR Spectroscopy*, Vol. *97* (Ed.: G. A. Webb), Academic Press **2019**, pp. 1–82.
[62] G. M. Scheuermann, L. Rumi, P. Steurer, W. Bannwarth, R. Mülhaupt, *J. Am. Chem. Soc.* **2009**, *131*, 8262–8270.
[63] G. D. Qi, Q. Wang, J. Xu, F. Deng, *Chem. Soc. Rev.* **2021**, *50*, 8382–8399.
[64] A. G. M. Rankin, J. Trébosc, F. Pourpoint, J.-P. Amoureux, O. Lafon, *Solid State Nucl. Magn. Reson.* **2019**, *101*, 116–143.
[65] T. Gutmann, J. Liu, N. Rothermel, Y. Xu, E. Jaumann, M. Werner, H. Breitzke, S. T. Sigurdsson, G. Buntkowsky, *Chem. - Eur. J.* **2015**, *21*, 3798–3805.
[66] A. J. Rossini, A. Zagdoun, M. Lelli, A. Lesage, C. Copéret, L. Emsley, *Acc. Chem. Res.* **2013**, *46*, 1942–1951.
[67] I. B. Moroz, M. Leskes, *Annu. Rev. Mater. Res.* **2022**, *52*, 25–55.
[68] G. Buntkowsky, M. Vogel, *Molecules* **2020**, *25*, 3311.
[69] N. B. Haro Mares, M. Brodrecht, T. Wissel, S. C. Döller, L. Rösler, H. Breitzke, M. M. Hoffmann, T. Gutmann, G. Buntkowsky, *J. Phys. Chem. C* **2023**, *127*, 19735–19746.
[70] S. C. Döller, M. Brodrecht, T. Gutmann, M. Hoffmann, G. Buntkowsky, *J. Phys. Chem. C* **2023**, *127*, 12125–12134.
[71] S. C. Döller, T. Gutmann, M. Hoffmann, G. Buntkowsky, *Solid State Nucl. Magn. Reson.* **2022**, *122*, 101829.
[72] G. Buntkowsky, S. Döller, N. Haro-Mares, T. Gutmann, M. Hoffmann, *Z. Phys. Chem.* **2022**, *236*, 939–960.
[73] M. Werner, N. Rothermel, H. Breitzke, T. Gutmann, G. Buntkowsky, *Isr. J. Chem.* **2014**, *54*, 60–73.
[74] G. Buntkowsky, H. Breitzke, A. Adamczyk, F. Roelofs, T. Emmler, E. Gedat, B. Grünberg, Y. Xu, H.-H. Limbach, I. Shenderovich, A. Vyalikh, G. Findenegg, *Phys. Chem. Chem. Phys.* **2007**, *9*, 4843–4853.
[75] X. Wang, K. S. K. Lin, J. C. C. Chan, S. Cheng, *J. Phys. Chem. B* **2005**, *109*, 1763–1769.
[76] R. K. Zeidan, S.-J. Hwang, M. E. Davis, *Angew. Chem.* **2006**, *118*, 6480–6483.
[77] C.-T. Tsai, Y.-C. Pan, C.-C. Ting, S. Vetrivel, A. S. T. Chiang, G. T. K. Fey, H.-M. Kao, *Chem. Commun.* **2009**, 5018–5020.
[78] A. E. Benett, C. M. Rienstra, M. Auger, K. V. Lakshmi, R. G. Griffin, *J. Chem. Phys.* **1995**, *103*, 6951–6958.
[79] R. B. Merrifield, *J. Am. Chem. Soc.* **1963**, *85*, 2149–2154.
[80] F. A. Stevie, C. L. Donley, *J. Vac. Sci. Technol. A* **2020**, *38*, 063204.
[81] R. Arrigo, M. E. Schuster, S. Abate, S. Wrabetz, K. Amakawa, D. Teschner, M. Freni, G. Centi, S. Perathoner, M. Hävecker, R. Schlögl, *ChemSusChem* **2014**, *7*, 179–194.
[82] R. Arrigo, M. E. Schuster, Z. Xie, Y. Yi, G. Wowsnick, L. L. Sun, K. E. Hermann, M. Friedrich, P. Kast, M. Hävecker, A. Knop-Gericke, R. Schlögl, *ACS Catal.* **2015**, *5*, 2740–2753.
[83] M. Tukhani, F. Panahi, A. Khalafi-Nezhad, *ACS Sustainable Chem. Eng.* **2018**, *6*, 1456–1467.
[84] J. Zhou, Y. Yang, L. Zhao, X. Li, R. Zhou, X. Zheng, *Front. Chem. China* **2009**, *4*, 142–148.
[85] M. Thommes, K. Kaneko, A. V. Neimark, J. P. Olivier, F. Rodriguez-Reinoso, J. Rouquerol, K. S. Sing, *Pure Appl. Chem.* **2015**, *87*, 1051–1069.

[86] M. Weigler, E. Winter, B. Kresse, M. Brodrecht, G. Buntkowsky, M. Vogel, *Phys. Chem. Chem. Phys.* **2020**, *22*, 13989–13998.
[87] P. I. Ravikovitch, A. V. Neimark, *J. Phys. Chem. B* **2001**, *105*, 6817–6823.
[88] M. L. Ojeda, J. M. Esparza, A. Campero, S. Cordero, I. Kornhauser, F. Rojas, *Phys. Chem. Chem. Phys.* **2003**, *5*, 1859–1866.
[89] J. Liu, C. Fasel, P. Braga-Groszewicz, N. Rothermel, A. S. Lilly Thankamony, G. Sauer, Y. Xu, T. Gutmann, G. Buntkowsky, *Catal. Sci. Technol.* **2016**, *6*, 7830–7840.
[90] A. Dos, V. Schimming, S. Tosoni, H.-H. Limbach, *J. Phys. Chem. B* **2008**, *112*, 15604–15615.
[91] T. Xu, J. Zhang, J. F. Haw, *J. Am. Chem. Soc.* **1995**, *117*, 3171–3178.
[92] B. Wehrle, J. Mortensen, H.-H. Limbach, J. Heinze, *Adv. Mater.* **1989**, *1*, 441–443.
[93] N. Popp, T. Homburg, N. Stock, J. Senker, *J. Mater. Chem. A* **2015**, *3*, 18492–18504.
[94] L. Carlton, B. Staskun, T. van Es, *Magn. Reson. Chem.* **2006**, *44*, 510–514.
[95] M. Allen, J. D. Roberts, *J. Org. Chem.* **1980**, *45*, 130–135.
[96] A. Ariza-Castolo, M. A. Paz-Sandoval, R. Contreras, *Magn. Reson. Chem.* **1992**, *30*, 520–526.
[97] M. P. Espe, B. R. Mattes, J. Schaefer, *Macromolecules* **1997**, *30*, 6307–6312.
[98] Z. D. Zujovic, G. A. Bowmaker, H. D. Tran, R. B. Kaner, *Synth. Met.* **2009**, *159*, 710–714.
[99] J. Liu, P. B. Groszewicz, Q. Wen, A. S. L. Thankamony, B. Zhang, U. Kunz, G. Sauer, Y. Xu, T. Gutmann, G. Buntkowsky, *J. Phys. Chem. C* **2017**, *121*, 17409–17416.
[100] J. Xiao, Z. Lu, Y. Li, *Ind. Eng. Chem. Res.* **2015**, *54*, 790–797.
[101] A. El-Faham, F. Albericio, *Chem. Rev.* **2011**, *111*, 6557–6602.
[102] L. Zhao, I. Smolarkiewicz, H.-H. Limbach, H. Breitzke, K. Pogorzelec-Glaser, R. Pankiewicz, J. Tritt-Goc, T. Gutmann, G. Buntkowsky, *J. Phys. Chem. C* **2016**, *120*, 19574–19585.
[103] I. G. Shenderovich, S. B. Lesnichin, C. Tu, D. N. Silverman, P. M. Tolstoy, G. S. Denisov, H.-H. Limbach, *Chem. - Eur. J.* **2015**, *21*, 2915–2929.
[104] M. Munowitz, W. W. Bachovchin, J. Herzfeld, C. M. Dobson, R. G. Griffin, *J. Am. Chem. Soc.* **1982**, *104*, 1192–1196.
[105] N. B. Haro Mares, S. C. Döller, T. Wissel, M. Hoffmann, M. Vogel, G. Buntkowsky, *Molecules* **2024**, *29*, 1669.

Manuscript received: September 02, 2024
Revised manuscript received: November 22, 2024
Accepted manuscript online: December 11, 2024
Version of record online: ■■, ■■